THE JANUS GEPAS MONOLAYER FOR EFFICIENT PHOTOCATALYTIC WATER SPLITTING

A THESIS SUBMITTED TO
THE GRADUATE SCHOOL OF ENGINEERING AND SCIENCE
OF BILKENT UNIVERSITY
IN PARTIAL FULFILLMENT OF THE REQUIREMENTS FOR
THE DEGREE OF
MASTER OF SCIENCE
IN
MATERIALS SCIENCE AND NANOTECHNOLOGY

By
Doğukan Hazar Özbey
August 2021

The Janus GePAs Monolayer for Efficient Photocatalytic Water Splitting
By Doğukan Hazar Özbey
August 2021

We certify that we have read this thesis and that in our opinion it is fully adequate, in scope and in quality, as a thesis for the degree of Master of Science.

Engin Durgun(Advisor)

Haldun Sevinçli

Seymur Jahangirov

Approved for the Graduate School of Engineering and Science:

Ezhan Karaşan
Director of the Graduate School

ABSTRACT

THE JANUS GEPAS MONOLAYER FOR EFFICIENT PHOTOCATALYTIC WATER SPLITTING

Doğukan Hazar Özbey
M.S. in Materials Science and Nanotechnology
Advisor: Engin Durgun
August 2021

The sun is considered an inexhaustible natural energy resource compared to fossil fuels. Regarding the limited amount of fuels such as coal and petroleum and their effect on nature, any application that has the ability to harvest the sunlight and produce energy becomes extremely important. One of the potential mechanisms that can remedy the energy demand in the future is photocatalysis, and two-dimensional (2D) materials with suitable electronic and optical properties offer new possibilities for photocatalytic applications. Although various 2D materials have hitherto been specified as adequate candidates, materials with high photocatalytic efficiency for water splitting are still minimal. In this regard, a novel 2D Janus GePAs monolayer is predicted and its capability for photocatalytic water splitting is examined by performing first-principles density functional theory. The GePAs monolayer is shown to possess robust dynamic and thermal stability. The direct electronic band gap in the visible region and band edge positions of the strain-free and strained monolayers are revealed to be convenient for redox reactions in wide pH ranges. The low recombination probability of charge carriers ensured by high and anisotropic carrier mobility enhances the material's photocatalytic potential. Optical response calculations, including many-body interactions, exhibit significant optical absorption capacity in the UV–visible range. Furthermore, ultra-low exciton binding energy facilitates dissociation into free electrons and holes, promoting photocatalytic reactions. Our study suggests GePAs monolayer is an ideal and remarkably promising material to be utilized in visible-light-driven photocatalytic applications.

Keywords: ab initio, density functional theory, Janus, photocatalysis, water splitting.

ÖZET

VERİMLİ FOTOKATALİTİK SU AYIRMA İÇİN İKİ-BOYUTLU JANUS GEPAS TEK KATMANLISI

Doğukan Hazar Özbey
Malzeme Bilimi ve Nanoteknoloji , Yüksek Lisans
Tez Danışmanı: Engin Durgun
Ağustos 2021

Güneş, fosil yakıtlara kıyasla tükenmez bir doğal enerji kaynağı olarak kabul edilir. Kömür ve petrol gibi yakıtların sınırlı miktarda olması ve bunların doğaya etkileri düşünüldüğünde, güneş ışığını toplama ve enerji üretme kabiliyetine sahip herhangi bir uygulama son derece önemli hale gelmektedir. Gelecekteki enerji talebini giderebilecek potansiyel mekanizmalardan biri fotokatalizdir ve uygun elektronik ve optik özelliklere sahip iki boyutlu (2B) malzemeler fotokatalitik uygulamalar için yeni olanaklar sunmaktadır. Bugüne kadar çeşitli 2B malzemeler uygun adaylar olarak belirtilmiş olsa da, su ayırma için yüksek fotokatalitik verimliliğe sahip malzemeler hala minimum düzeydedir. Bu bağlamda, yeni bir 2B Janus GePAs tek tabakası öngörülmekte ve ilk prensipler yoğunluk fonksiyoneli teorisi uygulanarak fotokatalitik su ayırma kabiliyeti incelenmektedir. GePAs tek tabakasının sağlam dinamik ve termal stabiliteye sahip olduğu gösterilmiştir. Gerilimsiz ve gergin tek tabakaların görünür bölgedeki doğrudan elektronik bant aralığı ve bant kenarı konumlarının, geniş pH aralıklarında redoks reaksiyonları için uygun olduğu ortaya çıkarılmıştır. Yüksek ve anizotropik taşıyıcı hareketliliği ile sağlanan yük taşıyıcılarının düşük rekombinasyon olasılığı, malzemenin fotokatalitik potansiyelini arttırır. Çok elektron etkileşimlerini içeren optiksel yanıt hesaplamaları, UV-görünür aralıkta önemli optik absorpsiyon kapasitesi sergiler. Ayrıca, ultra düşük eksiton bağlanma enerjisi, fotokatalitik reaksiyonları teşvik ederek serbest elektronlara ve deliklere ayrışmayı kolaylaştırır. Çalışmamız, GePAs tek tabakasının, görünür ışıkla çalışan fotokatalitik uygulamalarda kullanılmak üzere ideal ve oldukça umut verici bir malzeme olduğunu öne sürüyor.

Anahtar sözcükler: ab initio, yoğunluk fonksiyoneli teorisi, Janus, fotokataliz, su ayırma.

Acknowledgement

I would like to express my deepest gratitude to my supervisor Assist. Prof. Dr. Engin Durgun for his kind support and guidance so far. I am also grateful for the ideas, experiences, and joy that he conveyed during the last two years of my life. The pride I feel that is originated from my presence in his group will always be permanent same as the remembrance of pleasant days and nights at UNAM.

I am sincerely thankful for my old friend and groupmate Mert Miraç Çicek for his support and friendship. I would like to thank my friends Dr. Merve Demirtaş, Mirali Jahangirzadeh Varjovi, Mohammad Abboud, and Dr. Muammer Kanlı for being always kind and supportive.

I feel "Lucky" to meet dearest Gizem Mutlay and thankful for her love, support and gracefulness.

Without his existence, I would feel missing even I would not know what is missing. I am thankful to my only brother, Batuhan Tuna Özbey.

This thesis is dedicated to my mother and father, Rabia and Alpaslan, respectively. If I had a choice before I was born, I would definitely choose them.

Finally, thanks to all the notes that form the music which is a miracle that allows me to breathe.

The current study has been supported by the Scientific and Technological Research Council of Turkey (TUBITAK) under Project No. 117F383.

Contents

1 Introduction **1**

1.1 Overview of Two-dimensional Group IV-V Materials 3

1.2 Janus Monolayers 4

1.3 Photocatalytic Water Splitting 5

1.4 Motivation 6

1.5 Organization of the Thesis 7

2 Theoretical Background: Density Functional Theory **8**

2.1 Complexity of the Problem 10

2.2 Density Functional Theory 13

2.2.1 Hohenberg-Kohn Theorems 13

2.2.2 Kohn-Sham Approach 14

2.2.3 Exchange-Correlation Functionals 16

3 Results **18**

3.1 Structural Properties 18

3.2 Stability 19

3.3 Electronic Properties 22

3.4 The GePAs Monolayer Under Strain 25

3.5 Carrier Effective Mass and Mobility 29

3.6 Optical Absorbance 31

4 Conclusion **34**

A Details of Density Functional Calculations **45**

List of Figures

3.1 (a) Top and (b) side views of Janus GePAs monolayer. The unit cell is marked by dashed black rectangle. Thickness and bond lengths (red) are denoted in the figure and donated/accepted (+/−) charges are shown with relevant color codes. Germanium, phosphorus, and arsenic atoms are presented by blue, pink, and green spheres, respectively.) 19

3.2 The strain-energy curve of GePAs monolayer for uniaxial strain along the x- and y-directions, biaxial strain, and shear strain. . . 20

3.3 (a) Calculated phonon dispersion spectra of GePAs monolayer along high symmetry directions in Brillouin Zone. (b) The evolution of total energy during the AIMD simulations (lower panel) and the snapshots of the monolayer from side view at the end of each 3 ps (upper panel). The ground state energy at 0 K is displayed by the dashed blue line. 22

3.4 The electronic band structure and projected density of states (PDOS) of GePAs monolayer. The results for the PBE+SOC and HSE06+SOC are shown with solid blue and red dashed lines, respectively. The Fermi level is set to zero. 23

3.5 The electronic band structure of GePAs monolayer calculated by GGA-PBE and HSE06 functionals without the inclusion of SOC. . 24

3.6 (a) Representation of water splitting process using a semiconductor photocatalyst. (b) Band edge positions (VBM and CBM) of GePAs monolayer with respect to vacuum level. The redox potentials of water splitting are shown with black, red, and green dashed lines. 25

3.7 HSE06 band gaps (blue dots) and band edge positions for (a) uniaxial-x, (b) uniaxial-y, and (c) biaxial strains of GePAs monolayer with respect to the vacuum level under strain from –2% to +8%, respectively (negative/positive numbers refer to the compressive/tensile strain). The pink and blue colored bars represent the positions of the CBM and the VBM, respectively. The redox potentials of water splitting are shown in black, red, and green dashed lines.
26

3.8 The angle-dependent a) in-plane stiffness $Y^{2D}(\Theta)$ and b) Poisson's ratio $\nu(\Theta)$. 28

3.9 The angle-dependent effective mass of a) electrons m_e^* and b) holes m_h^*. 30

3.10 Frequency dependence of the a) real and b) imaginary parts of the complex dielectric constant. 32

3.11 Optical absorbance for incident light polarization along the x-(blue) and y-directions (pink). Energy range of visible light is given by the color spectrum in the plot. The band gap at the level of GW (E_g^{GW}) is denoted by dashed line. 33

List of Tables

3.1 Carrier effective mass m^* (m_0 is the mass of free electrons) along Γ–X and Γ–Y directions, deformation potential constant E_d in eV, and carrier mobility μ in ($cm^2V^{-1}s^{-1}$) of GePAs monolayer along the x- and y-directions. 31

Chapter 1

Introduction

Since the early years of the two-dimensional (2D) materials era, noteworthy advancements have been carried out in the discovery of post-graphene 2D nanostructures[1, 2, 3, 4, 5, 6]. Considerable interest in these materials explored with tremendous endeavors throughout the years bounds up with their remarkable properties, which mainly arise from the low dimensionality aspect of the structures. When dimensions are reduced to the nanoscale, in conjunction with lower interaction and symmetry effects, the behavior of materials can alter in a favorable way in terms of electrical conductivity, chemical reactivity, mechanical and optical properties. For instance, while graphite is very soft and slippery, graphene, on the other hand, becomes the strongest material ever known when exfoliated from its bulk form[7]. On the other hand, due to the quantum confinement feature, 2D materials can exhibit exciting physical phenomena which enable their potential usage in various technological applications, including optoelectronics[8], catalysis[9], energy storage[10], sensors[11], strain-engineered photonics[12] and even cancer therapy[13].

Amongst the growing family of 2D materials, some of them exhibit unique electronic properties that can be exploited to produce one of the cleanest energy sources, hydrogen. Photocatalytic water splitting is a promising strategy, which

can be operated directly by sunlight to generate hydrogen, offers an environment-friendly solution to the great energy demand of the present day and future. Apart from the specific suitability of certain 2D materials, they have several intrinsic properties of paramount importance. For instance, their high surface area compared to bulk materials allow 2D structures to contact sunlight at a significant level[14]. Moreover, the migration of photogenerated free charge carriers to the water interface is extremely fast due to the quantum confinement effect in conjunction with the apparent low dimensionality of the monolayers[15]. Additionally, a monolayer with directionally anisotropic transport properties brings about an efficient photocatalytic process due to the rapid separation and effective migration of photogenerated electron-hole pairs[16].

Considering all of the advantages mentioned above, 2D materials display a wide range of possibilities for better photocatalysts for hydrogen production purposes. However, the practically applicable materials for water splitting applications still lack due to efficiency issues. A theoretical contribution to this scientific effort plays a key role in remedying the mentioned issue. Density functional calculations are capable of determining of the thermodynamic and mechanical stability and estimating electronic properties, including band gap, band edges, carrier transport of a proposed material. In this regard, the main objective of this thesis is to explore a suitable and efficient material to assist the technological advancement of water splitting applications by exploiting computational methods.

In the following sections, an overview will be given for 2D Group IV-V materials. Subsequently, Janus monolayers and will be introduced, and general information about the photocatalytic water splitting process and related literature will be presented.

1.1 Overview of Two-dimensional Group IV-V Materials

Group IV-V compounds with formula MX (M = C, Si, Ge, Sn, Pb; X= N, P, As, Sb, Bi) have gained growing attention and have been intensively investigated both theoretically and experimentally[17, 18, 19, 20]. A subset of this class (SiP, SiAs, GeP, and GeAs) in bulk form belongs to the van der Waals (vdW) layered materials family with orthorhombic ($Cmc2_1$ for SiP) or monoclinic ($C2/m$ for GeP, GeAs, and SiAs) symmetries[21]. Generally, owing to the possibility of mechanical exfoliation, the realization of a vdW layered system can be regarded as a pioneering work for the isolation of 2D material. For this reason, the fabrication of bulk single crystals of group-IV monopnictides has made these materials even more attractive from a scientific point of view[21]. Accordingly, few-layer SiP nanoflakes have been successfully obtained by mechanical exfoliation methods, and its anisotropic nonlinear optical properties have been anticipated to possess great potential for future photonic integrated circuits and quantum chips [22]. Lately, following the synthesis of SiAs nanosheets, the production of a field-effect transistor (FET) and photodetector devices have been demonstrated. It has been shown that fabricated photodetector devices offer high photosensitivity with a strong anisotropy in the UV–visible domain [23]. Moreover, GeP nanoflakes have been synthesized from bulk, and photodetectors with highly anisotropic electronic transport and photoresponsivity have been realized[24, 25]. Based upon the same production procedure, Wang et al. have reported a 2D GeP-based photonic device in which they have exploited the strong nonlinear optical properties of GeP nanoflakes[26]. Likewise, few-layered GeAs nanosheets have been synthesized successfully, and a GeAs-based photoanode has been characterized as a promising candidate for high-performance optoelectronic nanodevices[27].

By considering the experimental progress on the group IV-V family, researchers

have concentrated significantly on 2D Ge-based binary structures due to their superior stability, earth-abundance, distinguished anisotropic properties, and tunable band gaps[28, 29, 30, 31, 32, 33, 34]. Predominantly owing to their low symmetry and having different bonding types along with different directions, GeP and GeAs systems in monolayer form have been predicted to exhibit anisotropic electronic, mechanical, and optical absorption characteristics. For instance, these semiconductors possess wide band gaps falling into the visible transmittance range with 2.08 (direct) and 2.31 (indirect) eV estimated by hybrid functional calculations, respectively[19]. Moreover, the anisotropic absorption coefficient of GeP and GeAs single-layers has been found to be higher compared to SiP and SiAs, and they have been suggested as promising candidates for solar water splitting[35].

1.2 Janus Monolayers

Even though structures obtained by top-down strategy encompass a significant portion of the field of 2D materials, synthetically produced monolayers have been realized with experimental endeavors, as well[36, 37, 38]. One of the intriguing derivatives of them is Janus monolayers designed by substituting all atoms at one side of their binary counterpart with a different atom. In these materials, since atoms on each facet have different atomic sizes and electronegativities, charge distributions on opposite sites are not equivalent, as well. This results in symmetry breaking, and due to the broken out-of-plane mirror symmetry by adding a third element, Janus monolayers can exhibit fascinating physical properties, or their capabilities can be enhanced concerning the prior structure. In 2013, the first experimental realization of a Janus graphene has become successful by modifying the graphene nonsymmetrically[39]. The centrosymmetric structure of the pristine graphene does not allow it to intrinsically exhibit piezoelectric characteristics. However, it is demonstrated in-plane, and out-of-plane piezoelectric responses can be induced to the possible Janus morphologies of graphene[40]. These exciting studies on Janus structures evoked an significant interest beyond graphene. These exciting studies on Janus structures evoked significant interest in the field of 2D materials. Following the fabrication of Janus graphene,

two research groups have synthesized Janus MoSSe monolayer by using a modified CVD method with different approaches. The realization of ternary MoSSe monolayers and their intrinsic vertical piezoelectric response underline the great potential of Janus materials[41, 42]. Apart from transition-metal dichalcogenides (TMD), various Janus structures have been predicted, and their potential usage for diverse applications has been investigated[43, 44, 45, 46].

1.3 Photocatalytic Water Splitting

Nanoengineered batteries, fuel cells, and catalysts may be able to leverage improved reactivity at the nanoscale to develop cleaner, safer, and more cost-effective energy production and storage methods. The advantage of increased surface area and enhanced reactivity in nanostructured materials allow them to be exploited in the development of better catalysts. One of the most potential solutions for long-term energy and environmental concerns is photocatalytic hydrogen generation via solar water splitting. Numerous experimental studies have demonstrated that the benefits of 2D materials can lead to an increase in photocatalytic activity compared to bulk materials[47, 48]. Various Janus 2D materials are anticipated to be effective photocatalysts for water splitting because of their adjustable band gaps, high specific surface area, and appropriate band edge locations with optimum redox potentials[49, 50, 51].

The electronic structure of the photocatalyst, which regulates the early phases of photocatalytic water splitting, is one of the crucial characteristics of photocatalytic water splitting. Incident light with adequate energy promotes an electron over the optical band gap of the photocatalysts, resulting in the formation of an electron-hole pair. Subsequently, the excited electron initiates the hydrogen reduction reaction to produce hydrogen, while the hole participates in the oxidation reaction for oxygen production. In order to classify a material as a photocatalyst, there are substantial requirements that should be fulfilled. Two indispensable factors are to possess a sufficient band gap higher than the free

energy of water splitting, which is 1.23 eV, and have appropriate band edge positions which must straddle the redox potential of water. On the other hand, a potential photocatalyst that will be utilized on an industrial scale should also be efficient. To achieve this, visible light absorption capability is of paramount importance. The capacity of photocatalytic water splitting materials to catch a substantial percentage of sunlight determines their effectiveness. A potential 2D material with a high optical absorption might have a high efficiency for photocatalytic water splitting. Moreover, excitonic effects are also decisive considering the necessary spatial separation of electron-hole pairs. A low exciton binding energy promotes the separation of excitons into free charge carriers, with which photocatalysis efficiency will improve. On the other hand, a 2D semiconductor photocatalyst must be insoluble in aqueous environments.

1.4 Motivation

Due to the fact that the layered structure of GeP and GeAs materials facilitates their production and possible functionalization, these structures, apart from other IV-V binary materials, are thoroughly examined in the literature.According to mentioned studies on 2D GeP and GeAs systems, they have been shown as noteworthy materials in various aspects. However, much more theoretical and experimental research is needed to offer a thorough understanding of the novel physics and phenomena that might emerge from Janus derivatives. Considering the emerging properties of GeP and GeAs monolayers given in the literature[18, 35], the possibility of obtaining material in Janus morphology with the potential to be an efficient photocatalyst drove our curiosity and motivated us to explore 2D Janus GePAs structure.

1.5 Organization of the Thesis

In this thesis, motivated by the aforementioned experimental and theoretical advancements and considering unique properties of GeP and GeAs systems, we designed Janus GePAs monolayer and unveiled its effective photocatalytic performance. Following the brief information about theoretical background based on first-principles density functional theory (DFT) in chapter 2, we started our analysis by examining the structural properties of the ground state configuration of GePAs monolayer in chapter 3. Subsequent to confirmation of its mechanical, dynamical, and thermal stability with elastic constants C, phonon spectra analysis, and *ab initio* molecular dynamics simulations (AIMD), respectively, we gave the electronic properties with band edge positions concerning the redox potential of the water. Next, we presented the variation of electronic bandgap and band edge positions of the monolayer with respect to applied strain, and we determined mechanical properties such as angle-dependent in-plane stiffness $Y^{2D}(\Theta)$ and Poisson's ratio $\nu(\Theta)$. Then we computed the carrier effective mass m^* and mobility μ in two directions reflecting the ability to inhibit recombination of electron-hole pairs. Lastly, taking into account many-body interactions, we expressed the optical response of the GePAs monolayer by the frequency dependence of the real and imaginary parts of the complex dielectric constant and optical absorbance capacity for incident light polarization along the x and y directions.

Chapter 2

Theoretical Background: Density Functional Theory

Revealing and understanding the physical properties of materials enables one to exploit them in various applications that can facilitate our lives. It is not a new practice, conversely, mankind is capable of researching materials' properties, comprehending their limits and "taming" to get benefit from them since early ages. For instance, after distinguishing differences of matters, ancient people understood that rocks could be sharpened and metals can be melted, and this knowledge became the foundation of what we call civilization today. Since those ages, our comprehension of the behavior of materials has changed dramatically as we discover how nature works. It has been required so much time and effort to figured out that the characteristics of materials and their response to external physical stimuli are originated from their elementary building blocks, which we know as atoms now.

When we enter the realm of atoms that make up the matter and electrons within, the governing law for these small particles is quantum mechanics. In this regard, one of the most profound scientific progress in history can be counted as the development of quantum mechanics with which one can trace down the origin of material properties up to atomic scale or nanoscale. From a materials science

point of view, quantum mechanical approach accounts for the results of complex interactions between atoms and the concept of physical properties are only the reflection of these interactions. However, the mentioned complexity impedes obtaining the full quantum mechanical description of material properties, and only for non-relativistic hydrogen-like systems can the exact solution be given. These kinds of elementary systems can be solved analytically by the Schrödinger equation, a linear partial differential equation that treats particles as wave functions. Unless some momentous approximations are employed, practical usage of the Schrödinger equation is not possible. In order to model interactions between constituent atoms without prior knowledge and investigate realistic systems at the nanoscale, some sophisticated methods are required. At this point, simplifying the problem to a certain level without losing essential information about the systems that are examined is of importance. That kind of a theoretical approach without any usage of experimental data and only based on the basic theorems of quantum mechanics is known as *ab initio* or first-principles methods.

Ab initio methods allow one to avoid expensive experiments and serve as a predictive power in materials science and solid-state physics. On the other hand, it can provide a valuable information to explain and verify the experimental data. Various *ab initio* methods have been developed, which are beneficial and appropriate for certain cases. Among them, the density functional theory (DFT) has a great reputation due to its computational efficiency, complete transferability, and applicability to a wide range of materials. The success of DFT has brought notable popularity to its application in materials science and solid-state physics since the 1970s. Up to the present day, the theory has become a standard approach complementary to experimental studies on materials. Two historic publications which are considered as foundations of the theory have been presented by Pierre Hohenberg-Walter Kohn in 1964 [52] and Walter Kohn-Lu Jeu Sham in 1965 [53]. The Hohenberg-Kohn paper has shown that instead of the ground-state wave function, the ground-state electron density $\rho(\mathbf{r})$ equivalently defines the system and uniquely determines all of its properties, including ground state energy. Subsequently, Kohn and Sham have expressed that finding the right electron density can be achievable by solving a set of single-electron equations.

These revolutionary approaches have decreased the difficulty of the problem by removing the electronic wave function from the play, and they have been proven for years to be successful in quantum-mechanical modeling of a broad class of materials.

Considering that all the calculations throughout the thesis have been performed in the framework of first-principles density functional theory (DFT), this chapter is devoted to the fundamentals of the theory. After introducing the complexity of the problem and Born-Oppenheimer approximations, the Hartree-Fock method will be given. Lastly, brief information about DFT will be presented.

2.1 Complexity of the Problem

Erwin Schrodinger published a breakthrough paper which is considered as the foundation of wave mechanics in 1926. In these times, it was understood that small particles could only be defined as a wave, and a wave function could contain all the information about the particle. In his paper, he introduced a wave-equation and its application to the hydrogen atom[54]. Apart from the hydrogen, when a system contains two or more electrons, one needs to deal with the many-body Schrödinger equation which has a naive presentation as the following:

$$\hat{H}\Psi_i(\mathbf{r},\mathbf{R}) = E_i\Psi_i(\mathbf{r},\mathbf{R}) \tag{2.1}$$

.

$\hat{H}$, ψ and E denote Hamiltonian operator, wave function and eigenvalue of the Hamiltonian, which is the energy of the system, and $\mathbf{r}$ and $\mathbf{R}$ define coordinates of electrons and nucleus as variables, respectively. The many-body Schrödinger equation, unfortunately, is extremely complex to solve. To express this, it is informative to present the terms involved in the Hamiltonian of a many-body system, which is in the following form:

$$\hat{H} = \sum_i \frac{\mathbf{p}_i^2}{2m} + \sum_I \frac{\mathbf{P}_I^2}{2M_I} - \sum_{i,I} \frac{Z_I e^2}{|\mathbf{r}_i - \mathbf{R}_I|} + \frac{1}{2} \sum_{i \neq j} \frac{e^2}{|\mathbf{r}_i - \mathbf{r}_j|} + \frac{1}{2} \sum_{I \neq J} \frac{Z_I Z_J e^2}{|\mathbf{R}_I - \mathbf{R}_J|} \quad (2.2)$$

where m and r_i $(i = 1, ..., N)$ correspond to mass and position of electrons and, M, R_I and Z_I $(I = 1, ..., N)$ represent mass, position and nuclear charge of nuclei, respectively. Terms in the Hamiltonian define kinetic energy of electrons, kinetic energy of nuclei, interaction between nuclei and electrons, interaction between electrons and interaction between nuclei, respectively.

In order to simplify this complexity, it is required to employ a number of approximations. The Born-Oppenheimer approximation is the assumption that the electronic motion and the nuclear motion in molecules can be separated. Firstly, due to the fact that nuclei are incomparably massive to electrons, their velocities are substantially lower. It means that electrons' response to the motion of the nucleus is instantaneous; hence they always take the ground state with respect to the nuclear configuration. The positions of the nuclei can be described as frozen from the electrons' point of view. This information allows one to decouple electrons' and nucleus' motion, which is called the Born–Oppenheimer approximation[55]. This approximation makes it possible to solve the electronic problem with fixed nuclei coordinates then moving them regarding the forces aroused from electronic and ionic distribution. However, this approach is still not enough to remove the complexity of the problem at the tractable level.

Another sight of the problem can be reflected by the computational complexity of solving the many-body Schrödinger equation. For a simple estimation, one can consider a real-space representation of the many-body wavefunction $\Psi = \Psi(\mathbf{r}_1, \mathbf{r}_2, ...\mathbf{r}_n)$ on a mesh discretized by using 10 mesh points to interpolate the wave function on each spatial coordinate. Thus, Ψ will be a function of 3n coordinates and 10^{3n} values are needed to define Ψ in real space. It means that to store the many-body wavefunction of an oxygen atom (n=8), one needs to store 10^{30} values on a computer. If we take 1 byte per value and 5×10^9 bytes per DVD, the amount of data will equal 2×10^{20} DVDs to store such a simple system.

It is clear that handling each particle dependant is not possible; instead, they should be thought of as independent particles, and their interactions with others should be taken in an averaged manner. To bring the problem down to the desired level, in 1928, Douglas R. Hartree proposed a method to handle the electronic problem[56]. The suggested approximation postulates that the wave function of the many-body system can be treated as the product of one-electron wave functions ($\Psi = \Psi_1 \times \Psi_2 \times .....\Psi_n$), which satisfies the single-particle Schrödinger equation in an effective field. This procedure introduced by Hartree is known as the self-consistent field method aiming to solve the wave equation as follows:

$$\left(-\frac{1}{2}\nabla^2 + U_{ext}(\mathbf{r}) + U_H(\mathbf{r}) \right)\Psi(\mathbf{r}) = E\Psi(\mathbf{r}) \tag{2.3}$$

where U_{ext} is the attractive potential between electrons and nuclei. U_H term is called Hartree potential aroused from Coulomb interaction between each electron and the effective field. Taking the electrons independently, total energy becomes only the sum of n one-electron energies. However, since two important principles of quantum mechanics, namely anti-symmetry and Pauli's exclusion principle, are not taken into account, this method allows obtaining only a crude estimation of the energy.

Hartree's method was refined with the inclusion of the anti-symmetry principle, and the wave function was expressed better with writing it as Slater determinant[57]. Being the simplest many-body system, the wave function of helium atom can be written as follows:

$$\Psi(\mathbf{r}_1, \mathbf{r}_2) = \frac{1}{\sqrt{2}} \begin{vmatrix} \Psi_1(\mathbf{r}_1) & \Psi_2(\mathbf{r}_1)) \\ \Psi_1(\mathbf{r}_2) & \Psi_2(\mathbf{r}_1) \end{vmatrix} = \frac{1}{\sqrt{2}}[\Psi_1(\mathbf{r}_1)\Psi_2(\mathbf{r}_2) - \Psi_2(\mathbf{r}_1)\Psi_1(\mathbf{r}_2)]$$

This refinement allows the wave function to contain antisymmetry property ($\Psi(\mathbf{r}_1, \mathbf{r}_2) = -\Psi(\mathbf{r}_2, \mathbf{r}_1)$); hence the effect of the exchange of two electrons' coordinates is taken into account correctly, while the many-body correlation is completely disregarded. The one-electron wave function in Slater determinant form

assures that the total wave function is antisymmetric, and with the inclusion of the exact exchange term to the wave function, the approach is known as the Hartree–Fock method. The original Hartree method can be considered an approximation to the Hartree–Fock method by neglecting exchange.

To conclude, the Hartree–Fock method makes five substantial simplifications when providing solutions for a many-body system.

- Assumptions have given by the Born–Oppenheimer approximation are still valid and play a key role in solutions of n-electron systems.
- Relativistic effects are entirely omitted and motion of the particles are assumed to be non-relativistic.
- Each energy eigenfunctions are described by a single Slater determinant.
- The mean-field approximation accounts for the electron exchange term; however, the electron correlation is neglected.
- The variational solution is considered to be a linear combination of a finite number of basis functions that follow orthogonality and normalization conditions.

2.2 Density Functional Theory

2.2.1 Hohenberg-Kohn Theorems

In 1964, Pierre Hohenberg and Walter Kohn presented two theorems with which DFT has been first put on a sound theoretical footing[52]. The connections between Hamiltonian, electron density, external energy, and wave function have been completed with these theorems.

The first theorem states that *the ground state energy determined by solving Schrödinger equation is a unique functional of the electron density.* With this

theorem, it can be concluded that the electron density alone can determine the external potential in a particular system at its ground state and vice versa. Moreover, due to the fact that the internal energy is independent of the system and there is no dependency on the external potential, a density-dependent internal energy should be as a universal functional of the electron density while its explicit formula is unknown. Thus, electron density defines the system's external potential, Hamiltonian, wave function, and all ground-state characteristics.

The second theorem, which is known as variational principle in the framework of DFT, states that *the electron density that minimizes the energy of the overall functional is the true electron density corresponding to the full solution of the Schrödinger equation*. This theorem provides a highly versatile and powerful way of determining ground-state energy and other characteristics. Fundamentally, it identifies a procedure for determining a system's minimum energy and demonstrates that the ground state of a system could be found using the variational principle. In other words, if the energy of the system is minimized with a varying electron density, the lowest energy reached will be ground-state energy, and the final electron density will be the actual ground-state density, correspondingly.

These two theorems have constituted the basis of the theory, and the incomplete electronic kinetic energy term problem, which results in unsuccessful attempts to exploit electron density, has been resolved by Walter Kohn and Lu Jeu Sham.

2.2.2 Kohn-Sham Approach

Considering Equation 2.3, the main problem arises from the coupled electron-electron interactions of the n-electron system, namely the Hartree potential given with the 3.term. Interactions between electrons are extremely complex, and their formulation is cumbersome. In order to overcome this difficulty, Kohn and Sham proposed substituting the kinetic energy of interacting electrons with the kinetic energy of a fictitious system non-interacting system[53]. Therefore, they found a way to map interacting n-electron systems on the non-interacting one-electron

systems under external energy.

All the interacting effects that is required to be considered to replace the n-electron system to one-electron system can be specified as kinetic(non-interacting+interacting), Hartree, exchange and lastly correlation energies. It should be noted that the correlation energy was absent in the Hartree-Fock method. The exchange-correlation energy contains all the unknown terms and is composed of exchange and correlation energies; and additionally, a contribution to correlation energy comes from electron(interacting) kinetic energy. Hence, the final expression of the total energy comprises four energy terms: electron(non-interacting) kinetic energy, external energy(due to the Coulombic electron-ion attraction), Hartree energy(due to the electron-electron repulsion) and exchange-correlation energy. In addition, the repulsive interaction energy between the nuclei is added as a constant, as the Born-Oppenheimer approximation suggests. Amongst them, only the exchange-correlation energy is not known and should be approximated.

Working with independent electrons rather than a complex interacting system facilitates the calculations. It can be deduced that this kind of sophisticated approach is able to mimic the real interacting system accurately.

The set of equations known as Kohn-Sham equations can be written as follows:

$$\left(-\frac{1}{2}\nabla^2 + U_{eff}(\mathbf{r}) \right) \Phi_i(\mathbf{r}) = \varepsilon_i \Phi_i(\mathbf{r}) \tag{2.4}$$

where $\mathrm{U}_{eff}(\mathbf{r}) = U_{ext}(\mathbf{r}) + U_H(\mathbf{r}) + U_{XC}(\mathbf{r})$.

Here, U_{eff} is the effective potential including three potential terms which are external, Hartree and exchange-correlation potentials, respectively. $\Phi_i(\mathbf{r})$ denotes Kohn-Sham orbitals which are the solutions of Kohn-Sham equations. These equations are solved self consistently.

2.2.3 Exchange-Correlation Functionals

2.2.3.1 Local Density Approximation(LDA)

One of the straightforward ways for treating the electron densities in a system is local density approximation(LDA). With this approximation, the complicated system is subdivided into numerous parts with uniform electron density with varying values. It is feasible to compute the exchange-correlation energy for each electron using the electron density assumed to be constant in that parts. The energies corresponding with these local components are added together to provide the overall exchange-correlation energy. Given that real systems are far from a homogeneous electron gas, the LDA works best in situations where the charge density fluctuates slowly, such as covalent systems and simple metals.

Some of the most common disadvantages of LDA functionals are:

- Since it underestimates the lattice parameters, calculations using LDA results in an overestimation in cohesive energy and the bulk modulus accordingly.
- LDA calculations give high adsorption energies and low diffusion barriers.
- LDA band gaps are usually found to be underestimated in most cases.
- It is unable to characterize transition metals with LDA.

2.2.3.2 Generalized Gradient Approximation(GGA)

As realistic systems are not homogeneous and are comprised of varying density landscapes near electrons, the generalized gradient approximation (GGA) can acquire local as well as semi-local information which implies the electron density and its gradient at a given point. When a system has rapidly changing charge density characteristics, the exchange correlation energy becomes extremely different compared to homogeneous electron gas. Despite in LDA, the error of the exchange

and correlation parts tends to compensate each other to a certain degree, GGA formalism becomes more appropriate to approximate the inhomogeneity of the electron density by taking the gradient and high order derivatives into account.

2.2.3.3 Hybrid Functionals

Although the GGA approach refines the bandgap underestimation problem of LDA at a certain level, inaccuracy in the calculation of the bandgap using GGA is still present and reaches up to 50% compared with experimental data. In order to overcome this problem, a specific combination of the Fock exchange and the GGA correlation is used, which is called hybrid functionals. Because the mixing of HF exchange energies provides a better cancelation of self-interaction, the use of hybrid functionals results in a wider band gap. However these functionals require much higher computational cost. On the other hand, due to the low screening that converts the nonlocal exchange term to the full Fock exchange term in wide gapped semiconductors, hybrid functional overestimate the gap. In contrast, the exchange term in moderate gapped semiconductors with intermediate screening can be compensated by a fractional amount of Fock exchange term.

Chapter 3

Results

3.1 Structural Properties

Inspired by the recent experimental studies of ternary monolayers and the synthesized 2D GeP and GeAs configurations, the GePAs structure is designed by substituting the topmost layer of the 2D GeP [19] with arsenic atoms. Following this substitution, Janus GePAs monolayer is characterized by the monoclinic C_s point group (Cm space group) with broken symmetries including rotation and inversion symmetry with respect to GeP and GeAs counterparts which belong to the C_{2h} point group ($C2/m$ space group). As illustrated in Fig. 3.1(a), the unit cell is rectangular with optimized lattice constants of a=3.70 Å, b=21.59 Å and consists of 12 germanium, 6 phosphorus, and 6 arsenic atoms. Our Bader charge analysis indicates that shared electrons are distributed in accordance with the electronegativity difference of respective atoms, as shown in Fig. 3.1(b).

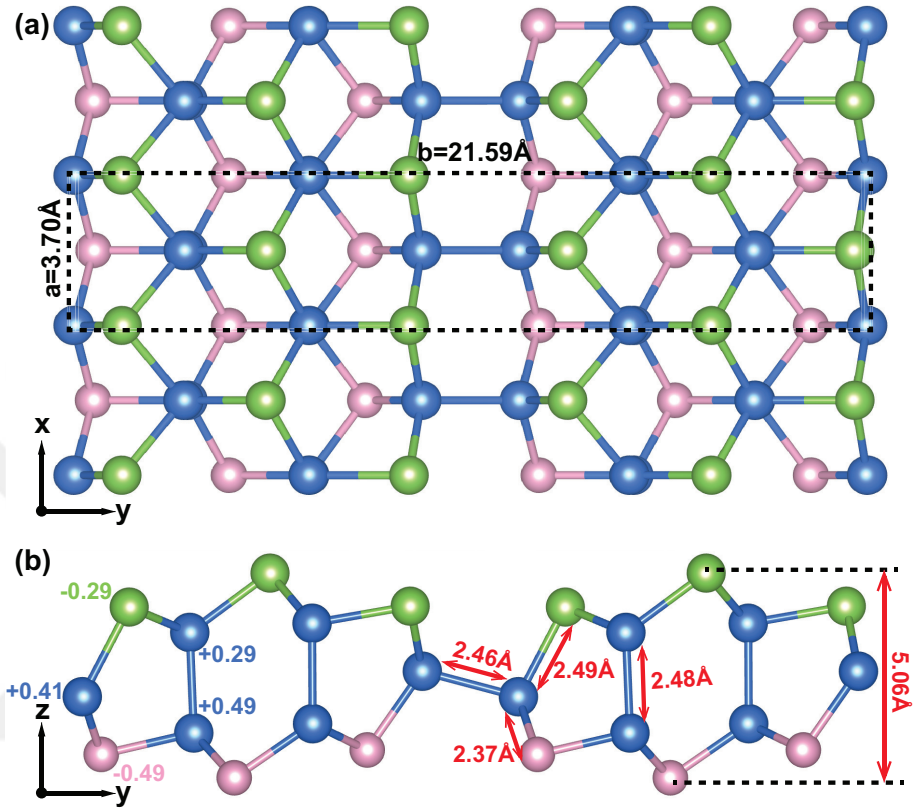

Figure 3.1: (a) Top and (b) side views of Janus GePAs monolayer. The unit cell is marked by dashed black rectangle. Thickness and bond lengths (red) are denoted in the figure and donated/accepted (+/−) charges are shown with relevant color codes. Germanium, phosphorus, and arsenic atoms are presented by blue, pink, and green spheres, respectively.)

3.2 Stability

Bond strength is an important parameter regarding the thermal stability of a material, which can be reflected by the cohesive energy. The cohesive energy per atom (E_{coh}) of GePAs monolayer is calculated as,

$$E_{coh} = \frac{E_{\mathrm{GePAs}} - 12 \times E_{\mathrm{Ge}} - 6 \times E_{\mathrm{P}} - 6 \times E_{\mathrm{As}}}{24}, \tag{3.1}$$

where E_{GePAs} is the total energy of GePAs monolayer; E_{Ge}, E_{P}, and E_{As} are the single atoms energy of respective elements. According to our calculations, the E_{coh} of GePAs (3.73 eV/atom) is in between the GeP (3.84 eV/atom) and GeAs (3.62 eV/atom) monolayers. Considering the experimental realization of

2D GeP and GeAs, E_{coh} indicates that Janus GePAs configuration is energetically favorable.

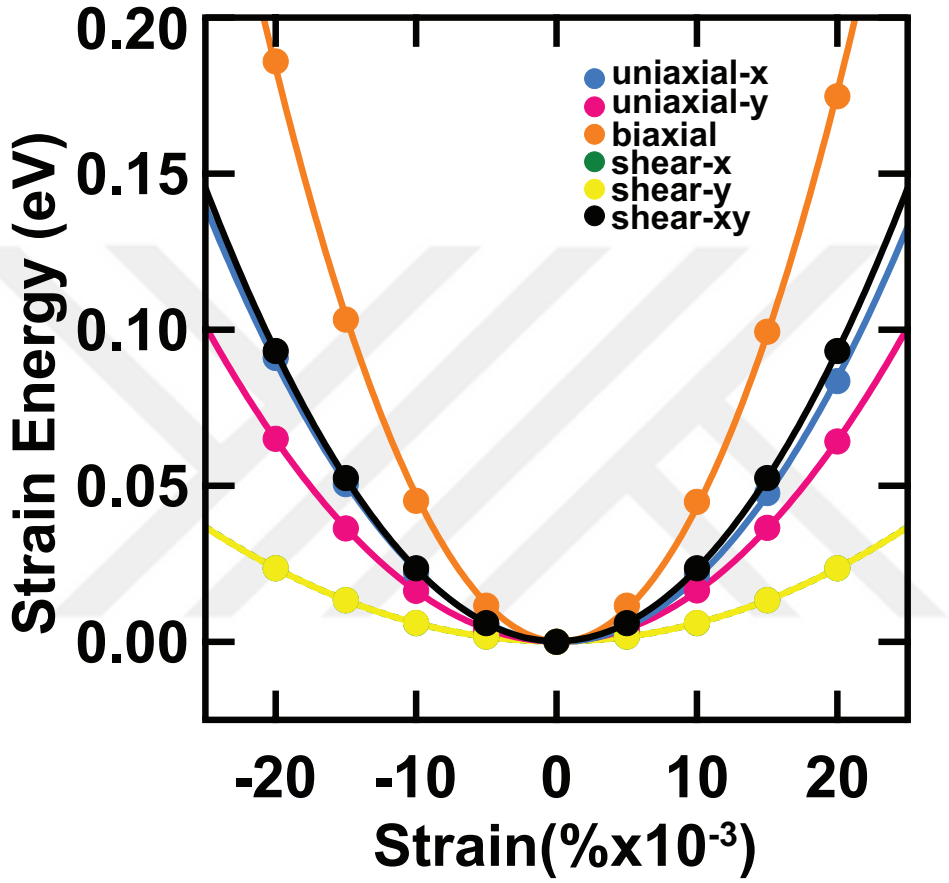

Figure 3.2: The strain-energy curve of GePAs monolayer for uniaxial strain along the x- and y-directions, biaxial strain, and shear strain.

The variation of the strain energy with the different types of applied strain was plotted in Fig. 3.3. The elastic constants C_{ij} were obtained by fitting second derivatives of strain energy per unit area with respect to in-plane uniaxial, biaxial, and shear strains using the following equations:

$$E_s(\varepsilon) = \frac{1}{2}C_{11}\varepsilon_x^2 + \frac{1}{2}C_{22}\varepsilon_y^2 + C_{12}\varepsilon_x\varepsilon_y + 2C_{66}\varepsilon_{xy}^2 \tag{3.2}$$

$$E_s(\varepsilon) = \frac{1}{2} C_{11} \varepsilon_x^2 \qquad (\varepsilon_y, \varepsilon_{xy} = 0) \rightarrow \text{uniaxial} - \text{x} \tag{3.3}$$

$$E_s(\varepsilon) = \frac{1}{2} C_{22} \varepsilon_x^2 \qquad (\varepsilon_x, \varepsilon_{xy} = 0) \rightarrow \text{uniaxial} - \text{y} \tag{3.4}$$

$$E_s(\varepsilon) = (\frac{1}{2} C_{12} + \frac{1}{2} C_{22} + C_{12}) \varepsilon_x^2 \qquad (\varepsilon_x = \varepsilon_y, \varepsilon_{xy} = 0) \rightarrow \text{biaxial} - \text{y} \tag{3.5}$$

$$E_s(\varepsilon) = 2 C_{66} {\varepsilon_{xy}}^2 \qquad (\varepsilon_x, \varepsilon_y = 0) \rightarrow \text{shear} \tag{3.6}$$

where E_s is strain energy over unit area, ε_x and ε_y are uniaxial strain levels in $x-$ and $y-$directions, respectively. C_{11} and C_{22} were calculated in order of Equation 3.3 and 3.4 for uniaxial-x and -y strains where the strain was only applied along related directions with $\varepsilon_{x,y} = (l - l_0)/l_0$. In order to take Poisson's effect into account, when uniaxial strains were applied, the other side of the monolayer was relaxed until the stress on this side reaches zero. Moreover, C_{12} was obtained using Equation 3.5, where the equi-biaxial strain was applied to the GePAs monolayer. Lastly, C_{66} was calculated by Equation 3.6 with implementing shear strain to the structure. The elastic constants C_{11}, C_{22}, C_{12} and C_{66} were found as 87.32, 64.63, 14.25, and 23.28 N m^{-1}, respectively. The constants satisfy the Born-Huang criteria[58] with $C_{11}C_{22} - C_{12}^2 > 0$ and $C_{66} > 0$ expressions and confirm the mechanical stability of the GePAs monolayer.

Albeit the structural optimization and Born-Huang criteria provide essential conditions, they do not ensure dynamical stability. Therefore, phonon spectra analysis is performed, and the lack of imaginary modes in the phonon band structure, as shown in Fig. 3.3(a), demonstrates that the GePAs monolayer is dynamically stable. We further analyze the high-temperature stability by carrying out AIMD simulations, in which the monolayer is kept at 200 K, 400 K, and 600

K during a total of 9 ps simulation time with 1 fs time steps. Resultant snapshots demonstrate no bond breaking, and the total energy fluctuates around a certain value without a distinct drop during the simulation for considered temperatures, as given in Fig. 3.3(b). These findings indicate that the GePAs monolayer can maintain its crystalline form even at elevated temperatures.

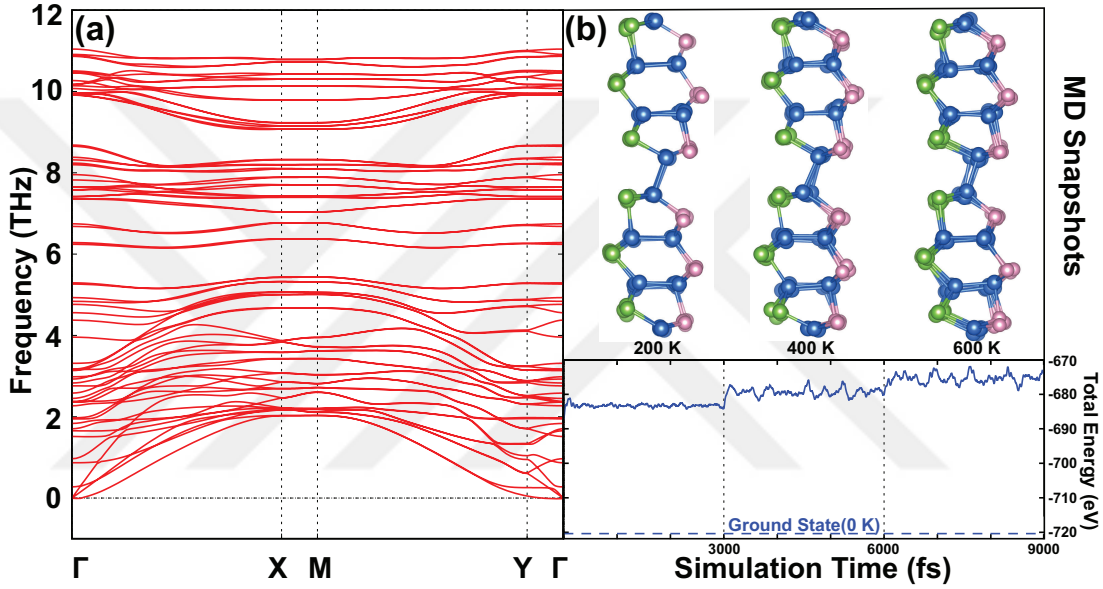

Figure 3.3: (a) Calculated phonon dispersion spectra of GePAs monolayer along high symmetry directions in Brillouin Zone. (b) The evolution of total energy during the AIMD simulations (lower panel) and the snapshots of the monolayer from side view at the end of each 3 ps (upper panel). The ground state energy at 0 K is displayed by the dashed blue line.

3.3 Electronic Properties

Having demonstrated its stability, we proceed to our examination with the electronic properties of the monolayer. The electronic band structure of GePAs monolayer calculated at the level of GGA-PBE and HSE06 with the inclusion of SOC are given in Fig. 3.4. The electronic band structures without SOC is also given in Fig. 3.5.

The HSE06+SOC calculations suggest that the GePAs monolayer is a direct

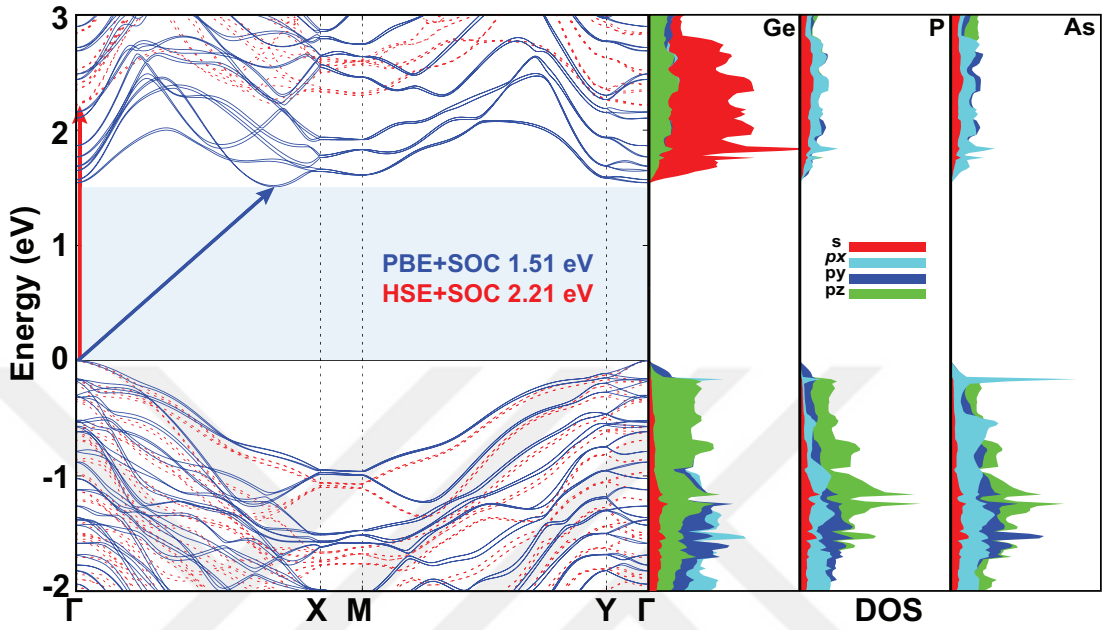

Figure 3.4: The electronic band structure and projected density of states (PDOS) of GePAs monolayer. The results for the PBE+SOC and HSE06+SOC are shown with solid blue and red dashed lines, respectively. The Fermi level is set to zero.

semiconductor with 2.21 eV band gap ($E_g^{\mathrm{HSE-SOC}}$). For comparison, the electronic structure of its binary counterparts was calculated and found that GeP monolayer has 2.41 eV quasi-direct $E_g^{\mathrm{HSE-SOC}}$ with 100 meV direct-indirect bandgap difference and GeAs has 2.07 eV direct $E_g^{\mathrm{HSE-SOC}}$. Different dispersion profiles of valance and conduction bands close to the Fermi level of GePAs can induce a high degree of in-plane anisotropy to electronic transport properties. The projected density of states (PDOS) of GePAs monolayer is also given in Fig. 3.4. The main contribution to conduction band minimum (CBM) comes from s orbitals of Ge atoms, while valence band maximum (VBM) is mostly composed of p_z orbitals of Ge, P, and As atoms. As illustrated in Fig. 3.6(a), a semiconductor with a band gap larger than 1.23 eV, which is the minimum Gibbs free energy required to split water, has the potential to be exploited as a photocatalyst. Even though numerous semiconductors meet the band gap criterion, their band alignments with respect to the redox potential of the water are not viable for photocatalytic applications. To test the mentioned fundamental requirement for photocatalytic water splitting, band edge positions are aligned with respect to the vacuum level.

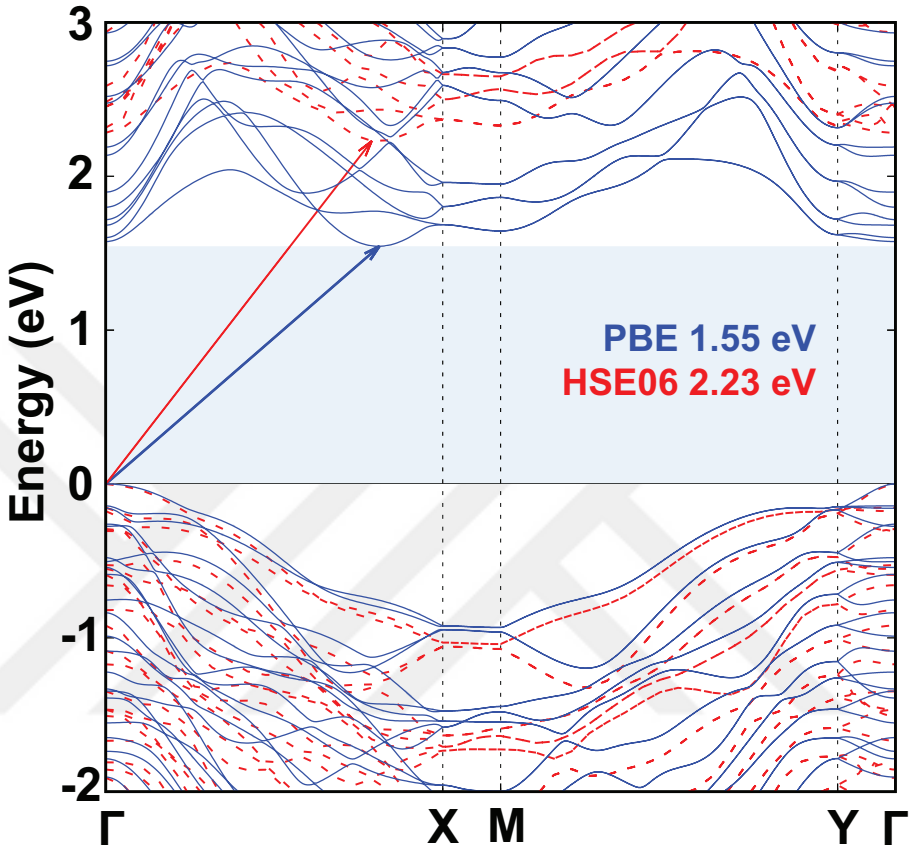

Figure 3.5: The electronic band structure of GePAs monolayer calculated by GGA-PBE and HSE06 functionals without the inclusion of SOC.

As depicted in Fig.3.6(b), the energy level of VBM (-5.86 eV) and CBM (-3.64 eV) of GePAs perfectly fit the redox potential of water. It is important to note that a competent catalyst should also operate in a wide pH range[59]. The redox potential of water splitting increases with pH, given with the Nerst equation [60]: $E_{H^+/H_2} = (-4.44 + \text{pH x } 0.059)$ eV and $E_{O_2/H_2O} = (-5.67 + \text{pH x } 0.059)$. As demonstrated in Fig. 3.6(b), the $E_g^{\text{HSE}-\text{SOC}}$ of GePAs monolayer completely covers both the oxidation potential of O_2/H_2O and the reduction potential of H^+/H_2 throughout the full pH range, from pH=0(acidic) to pH=14(basic). This suggests that the GePAs monolayer is photocatalytically active for simultaneous production of hydrogen and oxygen even in extreme conditions.

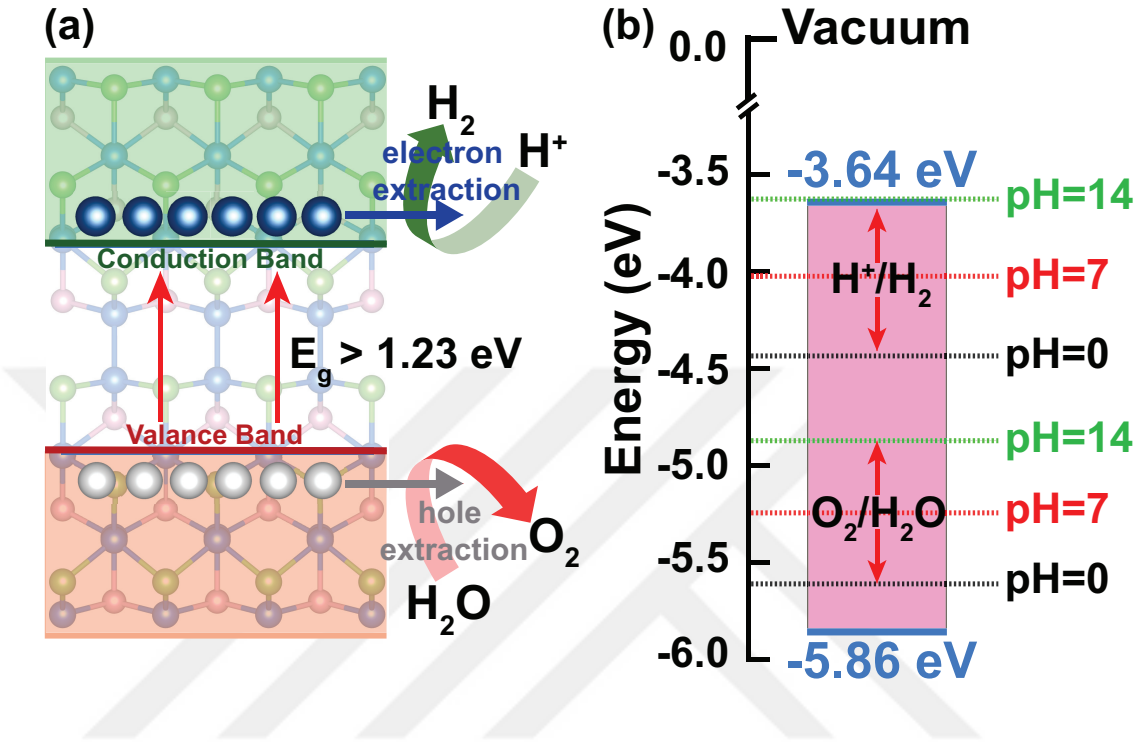

Figure 3.6: (a) Representation of water splitting process using a semiconductor photocatalyst. (b) Band edge positions (VBM and CBM) of GePAs monolayer with respect to vacuum level. The redox potentials of water splitting are shown with black, red, and green dashed lines.

3.4 The GePAs Monolayer Under Strain

Considering realistic applications, a semiconductor photocatalyst that maintains its functionality under strain is highly desirable. Therefore, we examined the band gap alteration and band alignment of GePAs monolayer with respect to applied uniaxial strain (in x- and y-directions) and biaxial strain. Fig. 3.7 exhibits the variation of the E_g^{HSE} with the band alignment of the -2% to +8% strained monolayers.

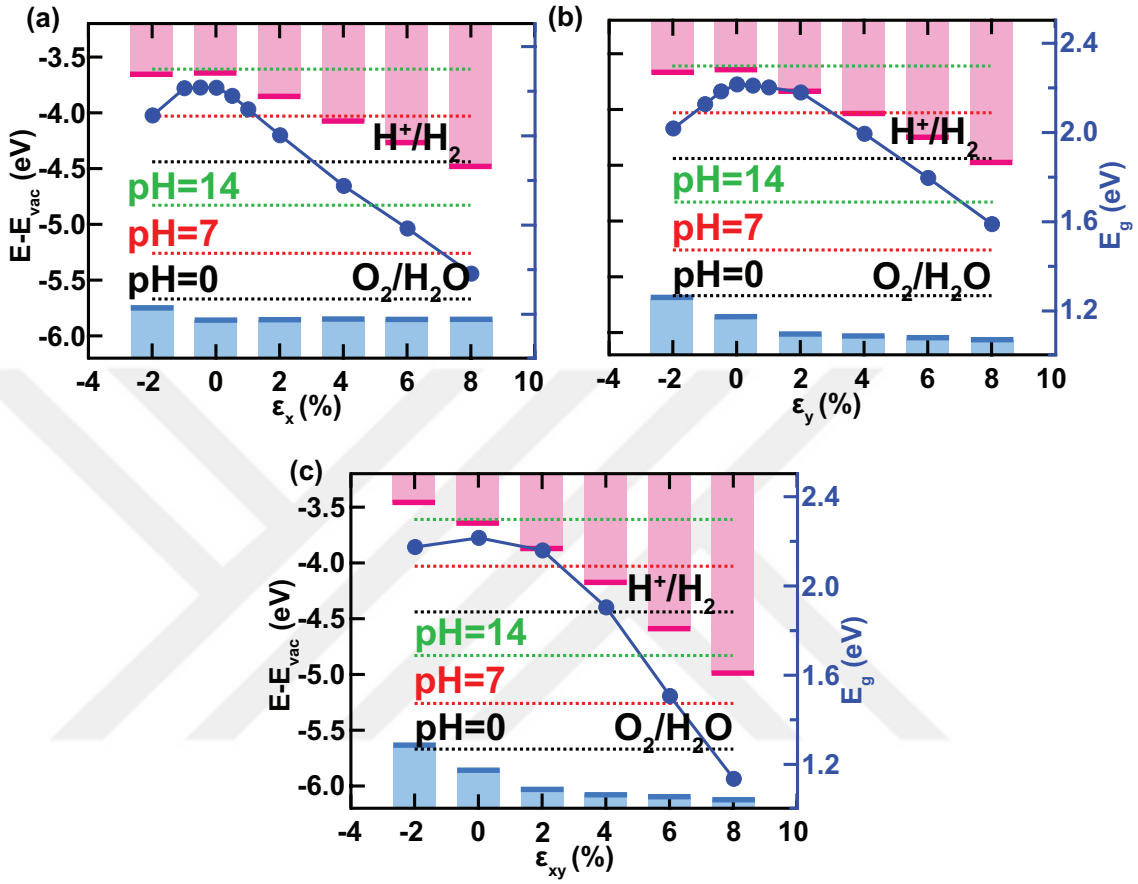

Figure 3.7: HSE06 band gaps (blue dots) and band edge positions for (a) uniaxial-x, (b) uniaxial-y, and (c) biaxial strains of GePAs monolayer with respect to the vacuum level under strain from –2% to +8%, respectively (negative/positive numbers refer to the compressive/tensile strain). The pink and blue colored bars represent the positions of the CBM and the VBM, respectively. The redox potentials of water splitting are shown in black, red, and green dashed lines.

Remarkably, E_g^{HSE}s of 2D GePAs under all uniaxial and biaxial strains (except +8% biaxial strain) are larger than 1.23 eV, and related band edge positions cover water redox potentials in wide pH ranges. These results indicate that GePAs monolayer can operate under practical compressive and tensile strain levels. In this manner, it is also worth mentioning the mechanical response of the system in the elastic regime. The in-plane elastic modulus $\mathrm{Y}^{\mathrm{2D}}(\Theta)$, which is a measure of tensile stiffness, is computed as 84 and 62 N m^{-1} along x- and y-axis, and indicates the flexibility of GePAs monolayer. Having soft elastic constants is an advantage in terms of strain engineering without inducing fracture[61].

$$Y_{2D}(\theta) = \frac{A}{C_{11}\ s^4\ +\ C_{22}\ c^4\ +\ (B\ -\ 2\ C_{12})\ c^2\ s^2} \tag{3.7}$$

$$v(\theta) = -\frac{(C_{11}\ +\ C_{22}\ -\ B\ )\ c^2\ s^2\ -\ C_{12}\ (c^4\ +\ s^4)}{C_{11}\ s^4\ +\ C_{22}\ c^4\ +\ (B\ -\ 2\ C_{12})\ c^2\ s^2} \tag{3.8}$$

where $c = cos(\theta)$, $s = cos(\theta)$, $A = (C_{11}\ C_{22}\ -\ C_{12}^2)$, and $B = (\frac{C_{11}\ C_{22}\ -\ C_{12}^2}{C_{66}})$.

In order to express the anisotropic mechanical behaviour of the structure we further investigated angle-dependent in-plane stiffness $\mathrm{Y}^{\mathrm{2D}}(\Theta)$ and Poisson's ratio $\nu(\Theta)$ according to the Equation 3.7 and 3.8, respectively[62]. The resultant plots can be seen in Fig. 3.8 (a) and (b)-. According to the given results, the high direction-dependency of the monolayer is evident and can be correlated to the different bonding environments in $x-$ and $y-$ directions.

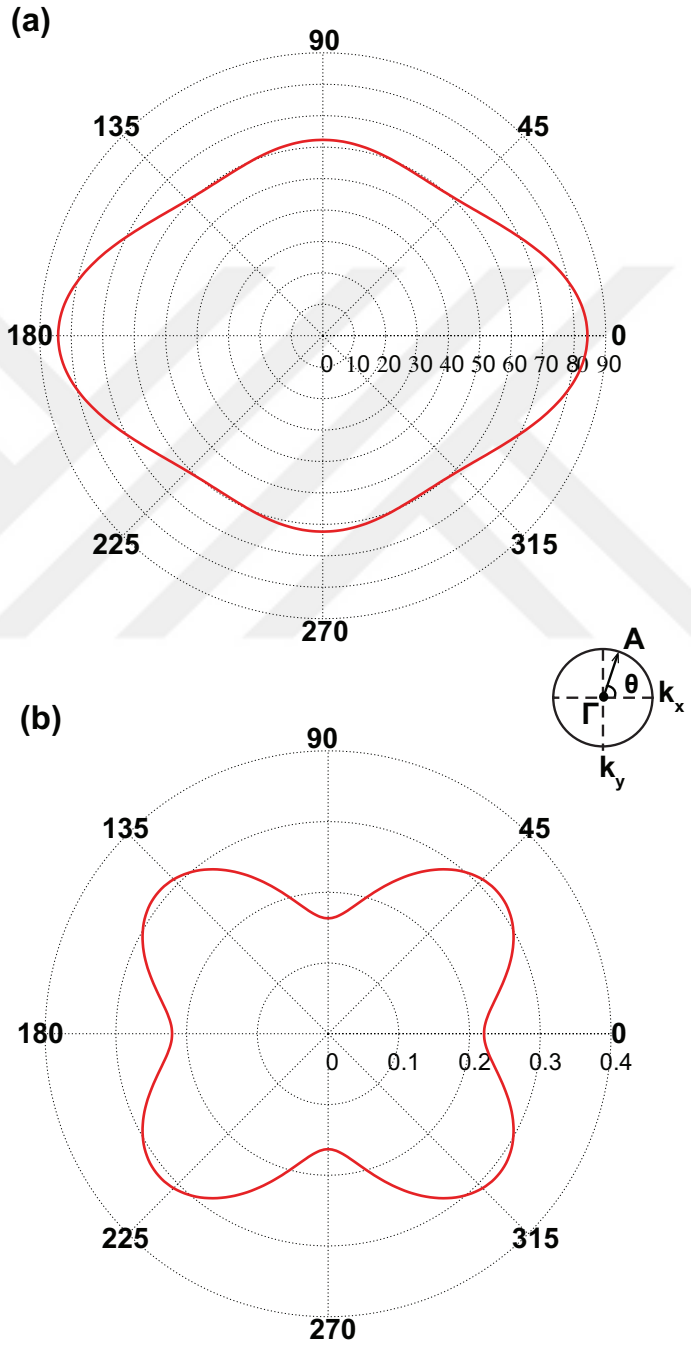

Figure 3.8: The angle-dependent a) in-plane stiffness $Y^{2D}(\Theta)$ and b) Poisson's ratio $\nu(\Theta)$.

3.5 Carrier Effective Mass and Mobility

A promising semiconductor to be exploited for photocatalytic water splitting should possess not only overall suitability but also exhibit high efficiency. As spatially discrete electrons and holes perform redox activities separately by the hydrogen reduction, $2H^+ + 2e^- \rightarrow H_2$ and oxidation, $H_2O + 2h^+ \rightarrow 1/2\ O_2 + 2H^+$ reactions, decrease in the recombination possibility of photogenerated charge carriers boost the photocatalytic performance[61]. Recombination of free electrons and holes can efficiently be suppressed if the catalyst offers highly anisotropic transport of charge carriers[63]. To investigate the migration ability of carriers, effective mass (m^*) and carrier mobility (μ) are calculated along the x- and y-directions of GePAs monolayer. The effective mass of electrons (m_e^*) and holes (m_h^*) are estimated by the quadratic fitting of the electronic band structure with the given expression: $m^* = \hbar(d^2E(k)/dk^2)^{-1}$ where $\hbar$ is the reduced Planck constant, k is wave vector and $E(k)$ is the energy with respect to k. To obtain μ, we calculate the deformation potential constant E_d; and using m^*, C, and E_d we get the room temperature carrier mobility for x- and y-directions (μ_x and μ_y) by using the formula within the deformation potential theory[64]: $\mu = eh^3C/(2\pi)^3 k_B T m^* m_d^* E_d^2$ where $m_d = \sqrt{m_x^* m_y^*}$ is the average effective mass, C is corresponding elastic constant, k_B is the Boltzmann constant and T is the temperature in Kelvin. Resultant values are summarized in Table 3.1 and angle-dependent m_e^* and m_h^* are illustrated in the Fig. 3.9.

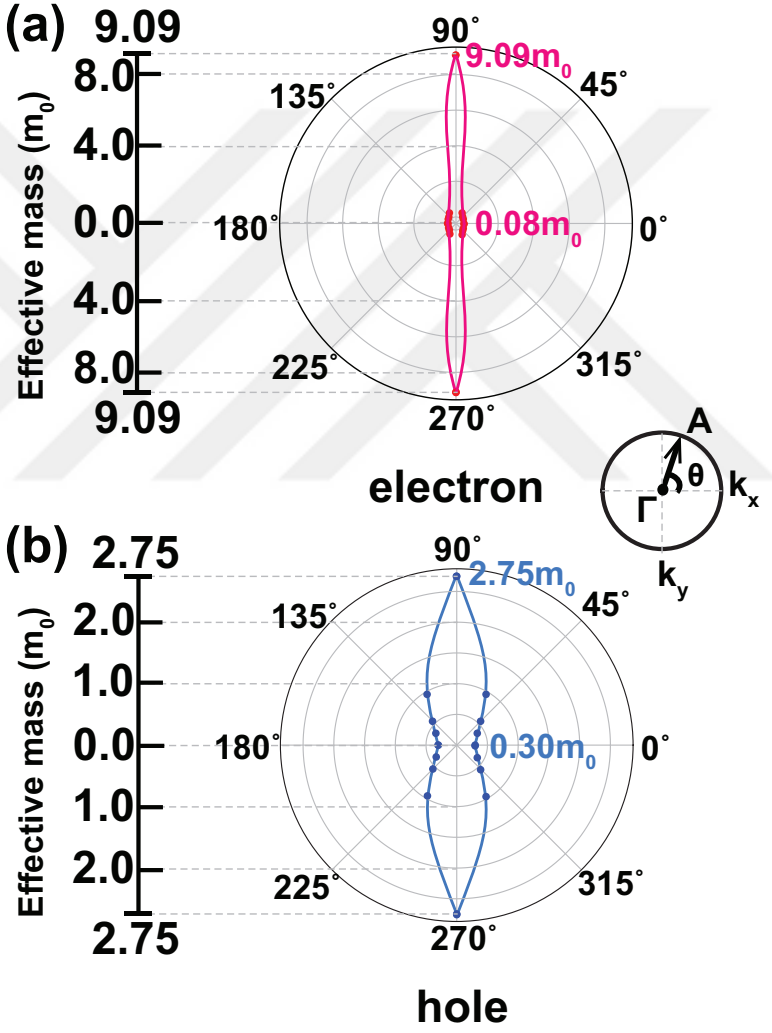

Figure 3.9: The angle-dependent effective mass of a) electrons m_e^* and b) holes m_h^*.

Table 3.1: Carrier effective mass m^* (m_0 is the mass of free electrons) along Γ–X and Γ–Y directions, deformation potential constant E_d in eV, and carrier mobility μ in ($cm^2V^{-1}s^{-1}$) of GePAs monolayer along the x- and y-directions.

	m_x^*/m_0	m_y^*/m_0	m_d^*/m_0	E_d^x	E_d^y	μ_x	μ_y
electron	0.08	9.09	0.85	0.59	8.83	7.78×10^4	2.28
hole	0.30	2.75	0.91	0.30	7.82	7.38×10^4	9.01

Taking the electronic band structure into account, the disparity in the curvature of the band dispersion throughout Γ–X and Γ–Y directions for both the lowest conduction band and the highest valence band is the indication of the anisotropic character of m^* and μ. The presence of light charge carriers along Γ–X direction with $m_{e,x}^*$=0.08m_0 and $m_{e,y}^*$=0.30m_0 stems from the available bonding environment of 2D GePAs in the x-direction, and gives rise to an extremely high mobilities with $\mu_{e,x}$=7.78x10^4 and $\mu_{h,x}$=7.38x10^4 $cm^2V^{-1}s^{-1}$, larger than the ultrahigh mobility of few-layered black phosphorus, which is shown to have μ=2.60x10^4 theoretically and $\backsim 10^3$ $cm^2V^{-1}s^{-1}$ experimentally[65]. On the other hand, the horizontal Ge-Ge bond in the y-direction behaves as a bottleneck for free-electron and -holes. The different dispersion profiles regarding Γ–X direction and low values of corresponding carrier mobilities in the y-direction can be attributed to this structural anisotropy. Consequently, the excellent migration capability of the GePAs monolayer with strong anisotropy facilitates the photogenerated carriers' motion and, therefore, boosts the photocatalytic efficiency.

3.6 Optical Absorbance

Since the primary strategy in visible-light-driven photocatalysis is to convert sunlight into chemical energy, the solar light absorption capacity of a photocatalyst plays a crucial role in improving efficiency. Moreover, weak exciton binding energy (E_b) enables charge carriers to be separated rapidly to improve the performance of the water-splitting process. To specify the optical absorption capability and exciton binding, we calculated the frequency-dependent imaginary dielectric

function ($\varepsilon(\omega) = \varepsilon_1(\omega) + i\varepsilon_2(\omega)$) and the optical absorbance for incident light polarization along x ($\mathbf{E}//\mathbf{x}$) and y ($\mathbf{E}//\mathbf{y}$) directions by taking into account the electron-hole correlations in Fig. 3.10 and Fig. 3.11, respectively.

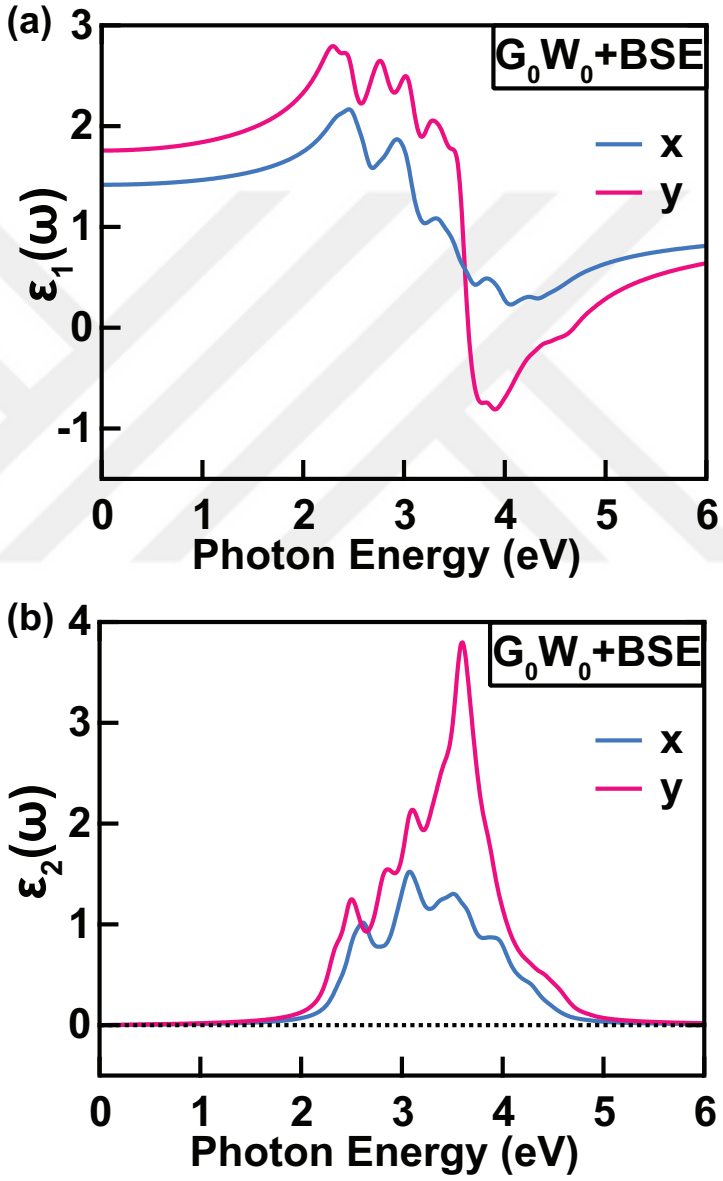

Figure 3.10: Frequency dependence of the a) real and b) imaginary parts of the complex dielectric constant.

The first prominent absorption peaks are observed in the mid-visible region, as shown in Fig. 3.11. The absorbance spectrum shows that a significant portion of light can also be captured from the ultraviolet region and the anisotropic nature

of the GePAs monolayer is much more pronounced in this region. Thus, the GePAs monolayer covers a broad absorption range with high absorbance ($\backsim 10^5$ cm^{-1}) and can be comparable to perovskite solar cells [66], supporting its superior properties in terms of water splitting reaction. In addition, E_b is obtained with respect to E_g^{GW} and found as 90 meV, which is weak and enhances the efficiency of the GePAs monolayer.

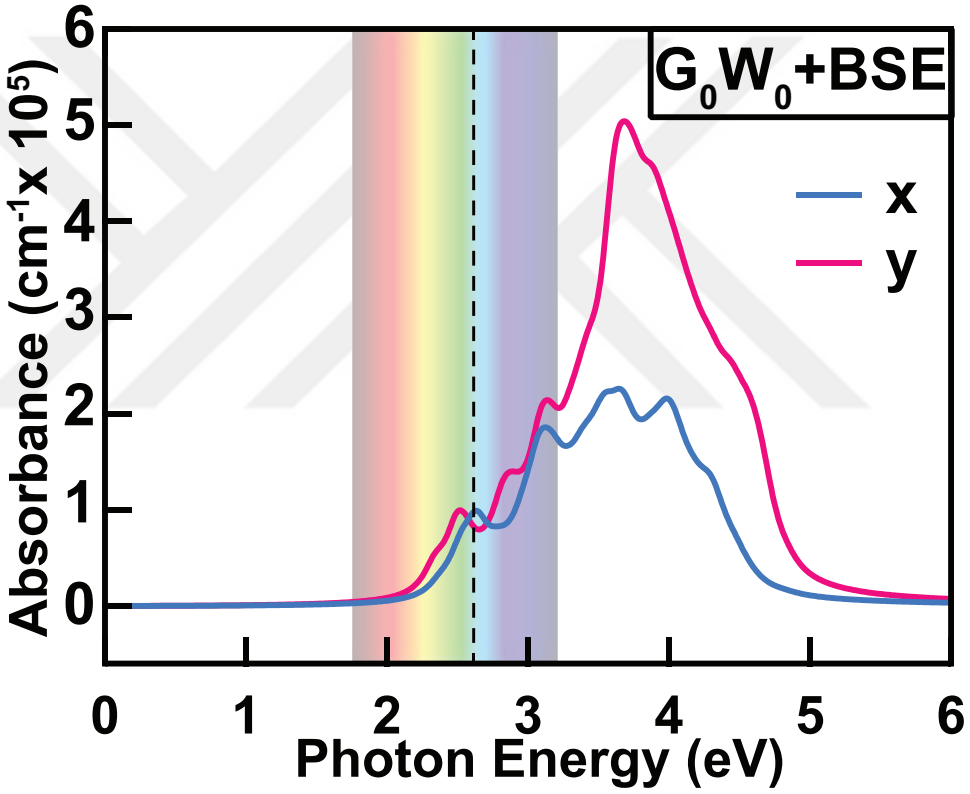

Figure 3.11: Optical absorbance for incident light polarization along the x- (blue) and y-directions (pink). Energy range of visible light is given by the color spectrum in the plot. The band gap at the level of GW (E_g^{GW}) is denoted by dashed line.

Chapter 4

Conclusion

In conclusion, motivated by recent experimental advancements in 2D GeP and GeAs materials, we designed Janus GePAs monolayer and revealed its unique properties within the scope of photocatalytic water splitting using first-principles DFT methods. In the beginning, we have shown by extensive analysis of mechanical, dynamical, and thermal stability using ab-initio phonon and finite temperature molecular dynamic simulations that free-standing GePAs monolayer is dynamically stable and can preserve its crystalline configuration even at high temperatures. After verifying its stability, the proposed system has been characterized as a direct band gap semiconductor using the HSE+SOC level of theory. Considering that one of the most fundamental requirements of a prospective photocatalyst is to have appropriate band edge positions with respect to the redox potential of the water, the GePAs monolayer's band edge suitability is remarkable. Accordingly, the examined structure has been shown to be operative for the simultaneous production of hydrogen and oxygen in mediums with a wide pH range. On the other hand, its behavior under applied strain has been inspected, and it has been shown that GePAs monolayer can operate under applicable strain levels (-2% to +8%). Additionally, the mechanical properties have been studied, and its flexibility that is beneficial in terms of photocatalytic applications, underlined. Furthermore, anisotropic and significantly high mobility ($\backsim 10^5 \mathrm{cm}^2\mathrm{V}^{-1}\mathrm{s}^{-1}$)

induce an excellent migration capability of the GePAs monolayer. In order to express optical characteristics that are decisive parameters regarding photocatalytic efficiency, GW calculations have been performed, taking excitonic effects into account. A high optical absorbance in the visible to UV part of the spectrum and weak exciton binding herald superior performance of GePAs monolayer as a photocatalyst. Consequently, within this thesis, we have shown by applying state-of-the-art computational methods that the Janus GePAs monolayer satisfies not only vital requirements of the water-splitting process but also offers high efficiency, thus unveiling it as an ideal material to be utilized in photocatalytic applications.

Bibliography

[1] F. Ersan, D. Keçik, V. Özçelik, Y. Kadioglu, O. Ü. Aktürk, E. Durgun, E. Aktürk, and S. Ciraci, "Two-dimensional pnictogens: A review of recent progresses and future research directions," *Appl. Phys. Rev.*, vol. 6, no. 2, p. 021308, 2019.

[2] Y. Liu, N. O. Weiss, X. Duan, H.-C. Cheng, Y. Huang, and X. Duan, "Van der waals heterostructures and devices," *Nat. Rev. Mater.*, vol. 1, no. 9, pp. 1–17, 2016.

[3] A. K. Geim and I. V. Grigorieva, "Van der waals heterostructures," *Nature*, vol. 499, no. 7459, pp. 419–425, 2013.

[4] F. A. Rasmussen and K. S. Thygesen, "Computational 2d materials database: electronic structure of transition-metal dichalcogenides and oxides," *J. Phys. Chem. C*, vol. 119, no. 23, pp. 13169–13183, 2015.

[5] P. Miró, M. Audiffred, and T. Heine, "An atlas of two-dimensional materials," *Chem. Soc. Rev.*, vol. 43, no. 18, pp. 6537–6554, 2014.

[6] Z. Lu, G. P. Neupane, G. Jia, H. Zhao, D. Qi, Y. Du, Y. Lu, and Z. Yin, "2d materials based on main group element compounds: phases, synthesis, characterization, and applications," *Adv. Funct. Mater.*, vol. 30, no. 40, p. 2001127, 2020.

[7] C. Lee, X. Wei, J. W. Kysar, and J. Hone, "Measurement of the elastic properties and intrinsic strength of monolayer graphene," *science*, vol. 321, no. 5887, pp. 385–388, 2008.

[8] S. Meng, T. Kong, W. Ma, H. Wang, and H. Zhang, "2d crystal–based fibers: Status and challenges," *Small*, vol. 15, no. 39, p. 1902691, 2019.

[9] R. Peng, L. Liang, Z. D. Hood, A. Boulesbaa, A. Puretzky, A. V. Ievlev, J. Come, O. S. Ovchinnikova, H. Wang, C. Ma, *et al.*, "In-plane heterojunctions enable multiphasic two-dimensional (2d) mos2 nanosheets as efficient photocatalysts for hydrogen evolution from water reduction," *ACS Catalysis*, vol. 6, no. 10, pp. 6723–6729, 2016.

[10] Y. Zhu, Z. Ju, X. Zhang, D. M. Lutz, L. M. Housel, Y. Zhou, K. J. Takeuchi, E. S. Takeuchi, A. C. Marschilok, and G. Yu, "Evaporation-induced vertical alignment enabling directional ion transport in a 2d-nanosheet-based battery electrode," *Adv. Mater.*, vol. 32, no. 10, p. 1907941, 2020.

[11] D. Tyagi, H. Wang, W. Huang, L. Hu, Y. Tang, Z. Guo, Z. Ouyang, and H. Zhang, "Recent advances in two-dimensional-material-based sensing technology toward health and environmental monitoring applications," *Nanoscale*, vol. 12, no. 6, pp. 3535–3559, 2020.

[12] N. Hussain, Y. Yisen, R. U. R. Sagar, T. Anwar, M. Murtaza, K. Huang, K. Shehzad, H. Wu, and Z. Wang, "Quantum-confined blue photoemission in strain-engineered few-atomic-layer 2d germanium," *Nano Energy*, vol. 83, p. 105790, 2021.

[13] H. Xie, Z. Li, Z. Sun, J. Shao, X.-F. Yu, Z. Guo, J. Wang, Q. Xiao, H. Wang, Q.-Q. Wang, *et al.*, "Metabolizable ultrathin bi2se3 nanosheets in imaging-guided photothermal therapy," *Small*, vol. 12, no. 30, pp. 4136–4145, 2016.

[14] B. Luo, G. Liu, and L. Wang, "Recent advances in 2d materials for photocatalysis," *Nanoscale*, vol. 8, no. 13, pp. 6904–6920, 2016.

[15] P. Niu, L. Zhang, G. Liu, and H.-M. Cheng, "Graphene-like carbon nitride nanosheets for improved photocatalytic activities," *Adv. Funct. Mater.*, vol. 22, no. 22, pp. 4763–4770, 2012.

[16] T. Su, Q. Shao, Z. Qin, Z. Guo, and Z. Wu, "Role of interfaces in two-dimensional photocatalyst for water splitting," *ACS Catal.*, vol. 8, no. 3, pp. 2253–2276, 2018.

[17] B. Özdamar, G. Özbal, M. N. Çınar, K. Sevim, G. Kurt, B. Kaya, and H. Sevinçli, "Structural, vibrational, and electronic properties of single-layer hexagonal crystals of group iv and v elements," *Phys. Rev. B*, vol. 98, no. 4, p. 045431, 2018.

[18] M. Ashton, S. B. Sinnott, and R. G. Hennig, "Computational discovery and characterization of polymorphic two-dimensional iv–v materials," *Appl. Phys. Lett.*, vol. 109, no. 19, p. 192103, 2016.

[19] A.-Q. Cheng, Z. He, J. Zhao, H. Zeng, and R.-S. Chen, "Monolayered silicon and germanium monopnictide semiconductors: excellent stability, high absorbance, and strain engineering of electronic properties," *ACS Appl. Mater. Interfaces*, vol. 10, no. 6, pp. 5133–5139, 2018.

[20] S. Zhang, S. Guo, Y. Huang, Z. Zhu, B. Cai, M. Xie, W. Zhou, and H. Zeng, "Two-dimensional sip: an unexplored direct band-gap semiconductor," *2D Mater.*, vol. 4, no. 1, p. 015030, 2016.

[21] C. Barreteau, B. Michon, C. Besnard, and E. Giannini, "High-pressure melt growth and transport properties of sip, sias, gep, and geas 2d layered semiconductors," *J. Cryst. Growth*, vol. 443, pp. 75–80, 2016.

[22] H. Sar, J. Gao, and X. Yang, "2d layered sip as anisotropic nonlinear optical material," *Sci. Rep.*, vol. 11, no. 1, pp. 1–8, 2021.

[23] D. Kim, K. Park, J. H. Lee, I. S. Kwon, I. H. Kwak, and J. Park, "Anisotropic 2d sias for high-performance uv–visible photodetectors," *Small*, vol. 17, no. 10, p. 2006310, 2021.

[24] L. Li, W. Wang, P. Gong, X. Zhu, B. Deng, X. Shi, G. Gao, H. Li, and T. Zhai, "2d gep: An unexploited low-symmetry semiconductor with strong in-plane anisotropy," *Adv. Mater.*, vol. 30, no. 14, p. 1706771, 2018.

[25] D. Kim, K. Park, F. Shojaei, T. T. Debela, I. S. Kwon, I. H. Kwak, J. Seo, J. P. Ahn, J. Park, and H. S. Kang, "Thickness-dependent bandgap and electrical properties of gep nanosheets," *J. Mater. Chem. A*, vol. 7, no. 27, pp. 16526–16532, 2019.

[26] Z. Wang, J. Guo, Y. Zhang, J. Liu, J. S. Ponraj, S. C. Dhanabalan, T. Zhai, X. Liu, Y. Song, and H. Zhang, "2d gep-based photonic device for near-infrared and mid-infrared ultrafast photonics," *Nanophotonics*, vol. 1, no. ahead-of-print, 2020.

[27] C. S. Jung, D. Kim, S. Cha, Y. Myung, F. Shojaei, H. G. Abbas, J. A. Lee, E. H. Cha, J. Park, and H. S. Kang, "Two-dimensional geas with a visible range band gap," *J. Mater. Chem. A*, vol. 6, no. 19, pp. 9089–9098, 2018.

[28] Y. Xu, H. Zhang, H. Shao, G. Ni, J. Li, H. Lu, R. Zhang, B. Peng, Y. Zhu, H. Zhu, *et al.*, "First-principles study on the electronic, optical, and transport properties of monolayer α-and β-gese," *Phys. Rev. B*, vol. 96, no. 24, p. 245421, 2017.

[29] X. Zhou, X. Hu, B. Jin, J. Yu, K. Liu, H. Li, and T. Zhai, "Highly anisotropic gese nanosheets for phototransistors with ultrahigh photoresponsivity," *Adv. Sci.*, vol. 5, no. 8, p. 1800478, 2018.

[30] J. Guo, Y. Liu, Y. Ma, E. Zhu, S. Lee, Z. Lu, Z. Zhao, C. Xu, S.-J. Lee, H. Wu, *et al.*, "Few-layer geas field-effect transistors and infrared photodetectors," *Adv. Mater.*, vol. 30, no. 21, p. 1705934, 2018.

[31] Z. Zhou, M. Long, L. Pan, X. Wang, M. Zhong, M. Blei, J. Wang, J. Fang, S. Tongay, W. Hu, *et al.*, "Perpendicular optical reversal of the linear dichroism and polarized photodetection in 2d geas," *ACS nano*, vol. 12, no. 12, pp. 12416–12423, 2018.

[32] A. Grillo, A. Di Bartolomeo, F. Urban, M. Passacantando, J. M. Caridad, J. Sun, and L. Camilli, "Observation of 2d conduction in ultrathin germanium arsenide field-effect transistors," *ACS Appl. Mater. Interfaces*, vol. 12, no. 11, pp. 12998–13004, 2020.

[33] G. Dushaq and M. Rasras, "Multilayer 2d germanium phosphide (gep) infrared phototransistor," *Opt. Express*, vol. 29, no. 6, pp. 9419–9428, 2021.

[34] Y. Yang, S.-C. Liu, Z. Li, D.-J. Xue, and J.-S. Hu, "In-plane anisotropic 2d ge-based binary materials for optoelectronic applications," *ChemComm*, vol. 57, no. 5, pp. 565–575, 2021.

[35] B. Mortazavi, M. Shahrokhi, G. Cuniberti, and X. Zhuang, "Two-dimensional sip, sias, gep and geas as promising candidates for photocatalytic applications," *Coatings*, vol. 9, no. 8, p. 522, 2019.

[36] A. J. Mannix, B. Kiraly, M. C. Hersam, and N. P. Guisinger, "Synthesis and chemistry of elemental 2d materials," *Nat. Rev. Chem.*, vol. 1, no. 2, pp. 1–14, 2017.

[37] L. Wang, P. Hu, Y. Long, Z. Liu, and X. He, "Recent advances in ternary two-dimensional materials: synthesis, properties and applications," *J. Mater. Chem. A*, vol. 5, no. 44, pp. 22855–22876, 2017.

[38] C. Zhang, Y. Nie, S. Sanvito, and A. Du, "First-principles prediction of a room-temperature ferromagnetic janus vsse monolayer with piezoelectricity, ferroelasticity, and large valley polarization," *Nano Lett.*, vol. 19, no. 2, pp. 1366–1370, 2019.

[39] L. Zhang, J. Yu, M. Yang, Q. Xie, H. Peng, and Z. Liu, "Janus graphene from asymmetric two-dimensional chemistry," *Nat. Commun.*, vol. 4, no. 1, pp. 1–7, 2013.

[40] M. T. Ong, K.-A. N. Duerloo, and E. J. Reed, "The effect of hydrogen and fluorine coadsorption on the piezoelectric properties of graphene," *J. Phys. Chem. C*, vol. 117, no. 7, pp. 3615–3620, 2013.

[41] J. Zhang, S. Jia, I. Kholmanov, L. Dong, D. Er, W. Chen, H. Guo, Z. Jin, V. B. Shenoy, L. Shi, *et al.*, "Janus monolayer transition-metal dichalcogenides," *ACS Nano*, vol. 11, no. 8, pp. 8192–8198, 2017.

[42] A.-Y. Lu, H. Zhu, J. Xiao, C.-P. Chuu, Y. Han, M.-H. Chiu, C.-C. Cheng, C.-W. Yang, K.-H. Wei, Y. Yang, *et al.*, "Janus monolayers of transition metal dichalcogenides," *Nat. Nanotechnol.*, vol. 12, no. 8, pp. 744–749, 2017.

[43] A. Kandemir and H. Sahin, "Janus single layers of in 2 sse: A first-principles study," *Phys. Rev. B*, vol. 97, no. 15, p. 155410, 2018.

[44] R. da Silva, R. Barbosa, R. R. Mancano, N. Duraes, R. B. Pontes, R. Miwa, A. Fazzio, and J. E. Padilha, "Metal chalcogenides janus monolayers for

efficient hydrogen generation by photocatalytic water splitting," *ACS Appl. Nano Mater.*, vol. 2, no. 2, pp. 890–897, 2019.

[45] R. Li, Y. Cheng, and W. Huang, "Recent progress of janus 2d transition metal chalcogenides: from theory to experiments," *Small*, vol. 14, no. 45, p. 1802091, 2018.

[46] M. Demirtas, M. J. Varjovi, M. M. Çiçek, and E. Durgun, "Tuning structural and electronic properties of two-dimensional aluminum monochalcogenides: Prediction of janus al 2 x x(x/x: O, s, se, te) monolayers," *Phys. Rev. Mater.*, vol. 4, no. 11, p. 114003, 2020.

[47] Y. Sun, H. Cheng, S. Gao, Z. Sun, Q. Liu, Q. Liu, F. Lei, T. Yao, J. He, S. Wei, *et al.*, "Freestanding tin disulfide single-layers realizing efficient visible-light water splitting," *Angew. Chem. Int. Ed.*, vol. 51, no. 35, pp. 8727–8731, 2012.

[48] Y. Sun, Z. Sun, S. Gao, H. Cheng, Q. Liu, J. Piao, T. Yao, C. Wu, S. Hu, S. Wei, *et al.*, "Fabrication of flexible and freestanding zinc chalcogenide single layers," *Nat. Commun.*, vol. 3, no. 1, pp. 1–7, 2012.

[49] J. Liu, X.-B. Li, D. Wang, H. Liu, P. Peng, and L.-M. Liu, "Single-layer group-ivb nitride halides as promising photocatalysts," *J. Mater. Chem. A*, vol. 2, no. 19, pp. 6755–6761, 2014.

[50] Y. Li, Y.-L. Li, C. M. Araujo, W. Luo, and R. Ahuja, "Single-layer mos 2 as an efficient photocatalyst," *Catal. Sci. Technol.*, vol. 3, no. 9, pp. 2214–2220, 2013.

[51] X. Zhang, B. Li, J. Wang, Y. Yuan, Q. Zhang, Z. Gao, L.-M. Liu, and L. Chen, "The stabilities and electronic structures of single-layer bismuth oxyhalides for photocatalytic water splitting," *Phys. Chem. Chem. Phys.*, vol. 16, no. 47, pp. 25854–25861, 2014.

[52] P. Hohenberg and W. Kohn, "Inhomogeneous electron gas," *Phys. Rev.*, vol. 136, no. 3B, p. B864, 1964.

[53] W. Kohn and L. J. Sham, "Self-consistent equations including exchange and correlation effects," *Phys. Rev.*, vol. 140, no. 4A, p. A1133, 1965.

[54] E. Schrödinger, "An undulatory theory of the mechanics of atoms and molecules," *Phys. Rev*, vol. 28, no. 6, p. 1049, 1926.

[55] M. Born and R. Oppenheimer, "Zur quantentheorie der molekeln," *Ann. Phys.*, vol. 389, no. 20, pp. 457–484, 1927.

[56] D. R. Hartree, "The wave mechanics of an atom with a non-coulomb central field. part i. theory and methods," in *Mathematical Proceedings of the Cambridge Philosophical Society*, vol. 24, pp. 89–110, Cambridge university press, 1928.

[57] J. C. Slater, "Note on hartree's method," *Phys. Rev.*, vol. 35, no. 2, p. 210, 1930.

[58] M. Born and K. Huang, *Dynamical theory of crystal lattices*. Clarendon press, Oxford, UK, 1954.

[59] X. Zou, X. Huang, A. Goswami, R. Silva, B. R. Sathe, E. Mikmeková, and T. Asefa, "Cobalt-embedded nitrogen-rich carbon nanotubes efficiently catalyze hydrogen evolution reaction at all ph values," *Angew. Chem.*, vol. 126, no. 17, pp. 4461–4465, 2014.

[60] V. Chakrapani, J. C. Angus, A. B. Anderson, S. D. Wolter, B. R. Stoner, and G. U. Sumanasekera, "Charge transfer equilibria between diamond and an aqueous oxygen electrochemical redox couple," *Science*, vol. 318, no. 5855, pp. 1424–1430, 2007.

[61] A. K. Singh, K. Mathew, H. L. Zhuang, and R. G. Hennig, "Computational screening of 2d materials for photocatalysis," *J. Phys. Chem. Lett.*, vol. 6, no. 6, pp. 1087–1098, 2015.

[62] E. Cadelano, P. L. Palla, S. Giordano, and L. Colombo, "Elastic properties of hydrogenated graphene," *Phys. Rev. B*, vol. 82, no. 23, p. 235414, 2010.

[63] Y. Xu, K. Xu, C. Ma, Y. Chen, H. Zhang, Y. Liu, and Y. Ji, "Novel two-dimensional β-gese and β-snse semiconductors: anisotropic high carrier mobility and excellent photocatalytic water splitting," *J. Mater. Chem. A*, vol. 8, no. 37, pp. 19612–19622, 2020.

[64] J. Bardeen and W. Shockley, "Deformation potentials and mobilities in non-polar crystals," *Phys. Rev.*, vol. 80, no. 1, p. 72, 1950.

[65] J. Qiao, X. Kong, Z.-X. Hu, F. Yang, and W. Ji, "High-mobility transport anisotropy and linear dichroism in few-layer black phosphorus," *Nat. Commun.*, vol. 5, no. 1, pp. 1–7, 2014.

[66] M. Shirayama, H. Kadowaki, T. Miyadera, T. Sugita, M. Tamakoshi, M. Kato, T. Fujiseki, D. Murata, S. Hara, T. N. Murakami, *et al.*, "Optical transitions in hybrid perovskite solar cells: ellipsometry, density functional theory, and quantum efficiency analyses for ch 3 nh 3 pbi 3," *Phys. Rev. Appl.*, vol. 5, no. 1, p. 014012, 2016.

[67] G. Kresse and J. Hafner, "Ab initio molecular dynamics for liquid metals," *Phys. Rev. B*, vol. 47, no. 1, p. 558, 1993.

[68] G. Kresse and J. Hafner, "Ab initio molecular-dynamics simulation of the liquid-metal–amorphous-semiconductor transition in germanium," *Phys. Rev. B*, vol. 49, no. 20, p. 14251, 1994.

[69] J. P. Perdew, K. Burke, and M. Ernzerhof, "Generalized gradient approximation made simple," *Phys. Rev. Lett.*, vol. 77, pp. 3865–3868, Oct 1996.

[70] P. E. Blöchl, "Projector augmented-wave method," *Phys. Rev. B*, vol. 50, no. 24, p. 17953, 1994.

[71] H. J. Monkhorst and J. D. Pack, "Special points for brillouin-zone integrations," *Phys. Rev. B*, vol. 13, no. 12, p. 5188, 1976.

[72] S. Grimme, "Semiempirical gga-type density functional constructed with a long-range dispersion correction," *J.Comput. Chem.*, vol. 27, no. 15, pp. 1787–1799, 2006.

[73] J. Heyd, G. E. Scuseria, and M. Ernzerhof, "Hybrid functionals based on a screened coulomb potential," *J. Chem. Phys.*, vol. 118, no. 18, pp. 8207–8215, 2003.

[74] A. V. Krukau, O. A. Vydrov, A. F. Izmaylov, and G. E. Scuseria, "Influence of the exchange screening parameter on the performance of screened hybrid functionals," *J. Chem. Phys.*, vol. 125, no. 22, p. 224106, 2006.

[75] D. Hobbs, G. Kresse, and J. Hafner, "Fully unconstrained noncollinear magnetism within the projector augmented-wave method," *Phys. Rev. B*, vol. 62, no. 17, p. 11556, 2000.

[76] R. Bader, "1997 polanyi award lecture why are there atoms in chemistry?," *Can. J. Chem.*, vol. 76, no. 7, pp. 973–988, 1998.

[77] G. Henkelman, A. Arnaldsson, and H. Jónsson, "A fast and robust algorithm for bader decomposition of charge density," *Comput. Mater. Sci*, vol. 36, no. 3, pp. 354–360, 2006.

[78] A. Togo and I. Tanaka, "First principles phonon calculations in materials science," *Scr. Mater.*, vol. 108, pp. 1–5, 2015.

[79] M. Shishkin and G. Kresse, "Implementation and performance of the frequency-dependent g w method within the paw framework," *Phys. Rev. B*, vol. 74, no. 3, p. 035101, 2006.

[80] E. E. Salpeter and H. A. Bethe, "A relativistic equation for bound-state problems," *Phys. Rev.*, vol. 84, no. 6, p. 1232, 1951.

Appendix A

Details of Density Functional Calculations

All calculations in this thesis were performed with the Vienna Ab initio Simulation Package (VASP)[67, 68] based on density functional theory (DFT). To approximate the exchange-correlation functional, the generalized gradient approximation with Perdew-Burke-Ernzerhof (GGA-PBE)[69] formalism was selected. The projected augmented wave method (PAW) with a plane-wave cutoff energy of 530 eV was used to take into account the ion-electron interactions [70]. The Brillouin zone (BZ) was sampled by Γ-centered $24 \times 4 \times 1$ k-point mesh within the Monkhorst-Pack scheme [71]. To avoid artificial interactions, vacuum space was set to $\backsim$ 15 Å, which was tested to be adequate. The Grimme method (DFT-D3) was applied to describe van der Waals (vdW) interactions[72]. The lattice parameters and atomic positions were relaxed until forces on the atoms were less than 0.01 eV/Å and the energy difference between two successive steps smaller than 10^{-5} eV. Being a well-known fact that GGA-PBE formalism underestimates the electronic band gaps, the Heyd-Scuseria-Ernzerhof (HSE06) hybrid functional approach was implemented to calculate a more accurate electronic band gap and band edges [73, 74]. The effect of spin-orbit coupling (SOC) was taken into consideration with the fully unconstrained noncollinear magnetic method [75] for both PBE and HSE06 levels. The charge transfer analysis among the atoms

was performed by using the Bader technique [76, 77]. Using $8 \times 1 \times 1$ supercell, phonon spectrum was obtained by the small displacement method implemented in the PHONOPY package[78]. The thermal stability was studied by performing *ab initio* molecular dynamics (AIMD) simulations during a total of 9 ps simulation time with 1 fs time steps. To examine the optical response of the system beyond the independent-particle approach, single-shot G_0W_0 approximation[79] was employed, and excitonic effects were treated by solving the Bethe-Salpeter equation (BSE)[80] within the Tamm–Dancoff approximation. For the G_0W_0 calculations, a k-point set of $18 \times 3 \times 1$ and cutoff energy of 320 eV were used, and the number of bands was increased to 144.